JET PROPULSION LABORATORY
CONTRACT #952 - 543

STUDY OF THE ZINC-SILVER OXIDE BATTERY SYSTEM

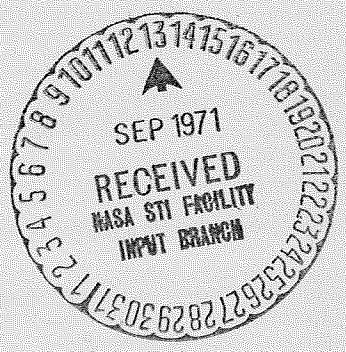

JET PROPULSION LABORATORY
CALIFORNIA INSTITUTE OF TECHNOLOGY
PASADENA, CALIFORNIA

QUARTERLY REPORT

APRIL - JUNE 1971

JET PROPULSION LABORATORY
CONTRACT #952 - 543

STUDY OF THE ZINC-SILVER OXIDE BATTERY SYSTEM

PRINCIPAL INVESTIGATOR
DR. LEONARD NANIS
ASSOCIATE PROFESSOR
SCHOOL OF CHEMICAL ENGINEERING
UNIVERSITY OF PENNSYLVANIA

This work was performed for the Jet Propulsion Laboratory, California Institute of Technology, sponsored by the National Aeronautics and Space Administration under Contract NAS7-100.

TABLE OF CONTENTS

SUMMARY

1.1 Reflectance at Porous Battery Electrodes

The development of an optical reflectance technique to monitor battery plate charge condition has been described extensively, with the emphasis on experimental problems being faced in the design of an optimal device with maximum resolution.

Preliminary experiments carried out with "Planté" plates of the lead-acid system indicated the suitability of the reflectance method, being able to clearly resolve the color and associated reflectance changes occurring with charging and discharging of positive battery plates.

Work is proceeding on adapting the reflectance method for pasted positives of the lead-acid type as a model electrode to monitor the penetration of reaction front through a porous electrode as a function of current density, time, porosity, etc.

1.2 Silver Oxide Electrode

Surface area of silver peroxynitrate, $Ag_7O_8 \cdot NO_3$, crystals was determined by B.E.T. method to be 0.1 m^2/gm, which is one thousand times greater than the external surface area. Previously, complete leaching to AgO product in just 1.5 hr at 100°C indicated some type of microporosity.

2.1 Membrane Permeation

Permeabilities of zincate ion through an acrylic-acid grafted and divinylbenzene cross-linked polyethylene membrane

have been examined at temperatures of 11°C, 17°C, 21.5°C and 27°C. The rotating permeation system permitted calculation of the mass transfer coefficients in the liquid boundary layers adjacent to the membrane. The solution side contributions to overall transport resistance amounted to a non-negligible 10%. The thickness of wet, swollen membrane at 25°C was found to be independent of the ZnO concentration (0 to 0.6M) in 40% KOH. Swelling amounted to 80% at 25°C. The mass transfer coefficient of the membrane was calculated from the measured overall permeation coefficient, the membrane thickness and the mass transfer coefficients through the boundary layers. This virtual membrane zincate diffusivity was 1.3×10^{-7} cm^2 sec^{-1} at 25°C (about one-fortieth of the free liquid diffusivity) with an activation energy of 6.6 Kcal per mol.

2.2 Capillary Diffusivity Model

A diffusion model assuming one dimensional diffusion in a capillary and three dimensional diffusion outside the capillary was set up for an assumed no-stirring condition. The equations were solved on a computer by the explicit finite difference method. The diffusivity of an electrolyte can be determined from the amount of electrolyte remaining in a capillary. When this remaining amount is fitted to the result based on stirring at the capillary mouth, the diffusivity so computed is always less than the correct value. For 50% remaining in the capillary where no stirring occurs, the "stirred" equation yields a diffusivity which is 30% too small.

2.3 Diffusivity Measurements

The capillary method with stirring has been checked by measuring the known integral diffusivity of 1N KCl into pure water. Flow was controlled to avoid any hydrodynamic end-error. The diffusivity at 25°C ±0.4°C was 1.74×10^{-5} cm^2 sec^{-1}, in fair agreement with the known value of 1.86×10^{-5} cm^2 sec^{-1}.

1. Electrode Studies

1.1 Porous Electrodes

1.1.1 Introduction

The optical luminance technique described in a previous report [1] has been improved and used for relative intensity measurements of diffusely reflected light from lead Planté plates and pasted positives in a lead-acid test cell. The diffuse reflectance of positive plates is followed during forming (charging) and discharging, where a significant color change occurs. Commercial universal oxide and expander (supplied by the National Lead Co.) is used for the pasting of the lead grids in the test cell.

1.1.2 Reflectance Theory

1.1.2.1 Diffuse Reflectance: If a beam of light is allowed to fall on the smooth surface of a solid material, two limiting cases arise: it is either reflected "specularly" (i.e., as from a mirror) or it is reflected in all directions of the hemisphere uniformly. In the first case, the surface is an ideal reflecting (polished) surface, while in the second, it is an ideal matte (scattering) surface. These two ideal limiting cases for a surface are never completely attained in practice. [2,4]

Diffuse reflectance from matte surfaces assumes that the density of the reflected radiation (surface brightness) is directionally independent (isotropy). This involves the validity

of the Lambert Cosine Law. Two conceptions are possible for the occurrence of this isotropic angular distribution: for particle diameters much greater than the wavelength, the radiation is partly reflected by means of regular reflection at elementary mirrors inclined statistically at all possible angles to the macroscopic surface. It also partly penetrates into the inside of the sample, where it then undergoes numerous reflections, refractions and diffractions at the irregularly located particles, finally emerging diffusely from the surface. For particle diameters of the order of the wavelength, scattering occurs. This scattered radiation is angularly distributed and is by no means isotropic. However, for a sufficiently large number and a sufficiently thick layer of closely packed particles, an isotropic scattering distribution can still be anticipated. A theoretical explanation for the diffuse reflection has not yet been proposed. [2] The choice of illumination and viewing geometry is dependent on the type of sample being considered. [3] Since for practical surfaces regular reflection is superimposed on diffuse reflectance, a distortion of the diffuse reflectance spectrum results which can be experimentally established using a goniophotometer.[2]

1.1.2.2 Standard of Reflectance: By far, the most important standard reference material for color measurement is the white standard of reflectance. For convenience, it is desirable that the reflectance of the standard be both greater than that of any substance to be measured and substantially independent of wave length over the entire visible spectrum. [5]

Freshly smoked MgO is recommended as a standard of reflectance.

The difficulty of preparing this standard reproducibly and its instability over time periods of even a few hours have led to the consideration of other materials as white working standards. The most widely available, reproducible and stable white reference material, adequately close in reflectance to freshly smoked MgO is pressed $BaSO_4$. It becomes, however, yellower and darker relatively slowly with time, while the rate of change decreases after about two days. [6]

1.1.3 Reflectance Technique

1.1.3.1 Introduction: Commercial instruments for the measurement of reflectance and reflection are divided into two groups: filter and monochromator devices. They consist generally of the following components: (a) light source; (b) monochromator or filter system; (c) sample container or attachment device; (d) light path or integrating component, such as a sphere or hemisphere; (e) detector, such as a photocell or photomultiplier tube; (f) visual or recording read-out device; and (g) reference or standard substance. [4]

Two of the most common types of reflectance or reflection-measuring instruments are illustrated in Figure 1 (see Sec. 1.1.5.1). [4] The commercially available reflectometers or spectral reflectometers were not directly suitable for a horizontal test cell arrangement. A simple device, based on the reflection type of arrangement, was chosen. A detailed description has been given in a previous report. [1]

1.1.3.2 Light Detection: Detectors that might be considered for measuring the reflectance include thermopiles, photocells, photodiodes, photomultipliers and photovoltaic cells.

Thermopiles can be excellent primary detecting devices, but are generally unsuitable for most laboratory and quality control types of service. Not only are they difficult to apply properly, but they are costly, lose their calibration when mishandled, and have an inadequate frequency response. [7]

Photodiodes have good frequency capabilities, are reasonably priced, and are being used in pulse and high-frequency applications. However, for our purpose the low-frequency conditions are important and therefore frequency response is not a critical sensor parameter. Because the photodiode must be electronically biased, a well-regulated bias supply is required to insure consistent results. [7]

Good sensitivity and frequency response plus a large detection area are some photomultiplier features. But multi-element phototubes are expensive, require high voltage supplies and, since output is a function of supply voltage, stability problems can arise. [7]

Photovoltaic cells, particularly the solar cell variety, have a large active area, good long-term stability,and good spectral matching, are easy to use and are inexpensive. The satisfactory frequency response,with the fact that power or bias supplies are not required, makes the solar cell most suitable for the diffuse reflection measurements. [7]

The silicon cell might be used either as an energy converter or as an intensity measuring device. Loferski and Wysocki [8]

showed that shallower junction depths would improve the blue response and Koltun and Golovner [9] described how antireflective coatings can improve blue response. Both of these techniques could be used to improve the silicon cell as a photometric detector. Little information is available on adapting the device to photometric measurements. The ability of silicon cells to produce either a linear response or a logarithmic response with respect to incident light level was already well-known. Witherell and Faulhaber [10]reviewed the characteristics of the silicon cell most important to photometric applications, including spectral response, linearity and temperature sensitivity, and a description of the silicon cell operation.

Although the silicon solar cell was developed for solar energy conversion, it has characteristics which make it well suited for photometric applications. It responds to visible radiation, can be made in convenient shapes and sizes, is stable, exhibits no fatigue or memory effects and, in short-circuit operation, has excellent linearity. Measurements on many solar cells show that the consistency of spectral response is far superior to that of phototubes.

1.1.4 Preliminary Experiments

In a new series of experiments, a glass beaker has been employed as a battery test cell placed on top of the dish of the reflectance device and surrounded by black paper. The cell contains a perforated lead foil charged with PbO_2 powder, and a

lead counter-electrode separated by a PVC ring in a 20% H_2SO_4 solution.

During discharge, the PbO_2 should be converted into $PbSO_4$, while a color change might take place from reflective black to dull brown. [11] However, no conversion of PbO_2 took place, due to non-electrical contact between the active material the perforated lead foil. The latter should function as a supporting grid for the active material. After the failure of the first attempt in making a porous electrode for the testing of the reflectance resolution of the employed optical device, it was obvious that a better approach would be to try to detect changes in the reflectance of a single lead foil plate (Planté plate) during formation (charging) and discharging.

1.1.4.1 Planté Experiments (I): The same arrangement and test cell has been used in the formation of the thin "Planté" plate. No standard of reflectance has been used because only the change of the reflectance was tested. First a charging and discharging had been carried out at 1 mA/cm^2 in 1.22 sp.gr. sulphuric acid. The change for the second charging cycle was about 11%. The color change was distinct, going from whitish grey to dull brown.

1.1.4.2 Pasted Plate Experiments (I): After the successful experiments with a thin lead Planté plate as positive, an attempt was made to manufacture a pasted positive as a porous model electrode.

A lead-antimony grid (thickness 1.5 mm) with 8% antimony has been pasted with active material of positive plates of an already used battery. After pasting, the plate was dried

for 60 hours at room temperature. The counter electrode consisted only of grid material. The plates in horizontal position were separated by a thin PVC ring separation and pressed to the bottom of the test cell. Charging and discharging had been performed, but the reflectance did not change. Visual observation did confirm the fact that only the grid of the pasted plate had been active, while active material remained unchanged.

1.1.4.3 Pasted Plate Preparation: In order to produce a positive which represented actual battery plate behavior, a pasting and forming method was devised following a recommended procedure in battery manufacture. [12]

1.1.4.3.1 Grid Material: The grids serve as support for the active material of the plates and conduct the electric current. The grids also have an important function in maintaining a uniform current distribution throughout the mass of active material. [13] The circular or square grids used in the test cell have been cut out from a real lead-antimony battery grid (12 x 14.3 cm) with straight cross bars across the plate, and are designed to lock the active material in place.

Using a hydraulic press, the thickness (initially 1.8 mm) is reduced to about 0.5 mm in some cases. Before pasting, lead strips as electrical connectors have been soldered to the grid and coated afterwards with acid-resistant black wax.

1.1.4.3.2 Pasting Process: Universal oxide of the National Lead Co. has been used as paste mixture for the positive plate. Expanders (National Lead Co.) are added in small amounts (ca. 2%) to the paste for making negative plates. [12] These are substances such as lampblack, barium sulfate (commonly called blanc fixe) and wood flour and organic extracts of wood. [13]

During preparation of the paste with dilute sulfuric acid, reactions occur that result in the formation of basic lead sulfate and the liberation of considerable heat. The temperature of the mixture rises to a maximum, so that cooling must be provided to avoid premature solidification before the paste can be applied to the grid. The lead sulfate is the cementing material which makes a firm plate. Many variations in the conditions of preparing and applying the paste are possible. Deviations in the physical and chemical characteristics of the oxides, the percentage true red lead which is present, the temperature and strength of the acid solution, the time of mixing, the treatment of the plate during and after the pasting process, and even the atmospheric humidity are among the conditions that affect the finished product. [13]

The usual procedure is to add a considerable portion of water to the oxides before adding a somewhat stronger solution of acid. The acid must be added slowly while mixing is continued under forced air cooling. A final portion of water is then added as required to bring the paste to the proper consistency. [12,13]

For the preparation of the pasted model electrodes, 12 grams of universal oxide were weighed out. Before the addition of H_2SO_4, 1.1 cm^3 water was mixed with the oxide. Then, 1.1 cm^3 sulfuric acid (1.40 sp.gr.) was added in drops under continuous forced air cooling. After the addition of about 0.5 cm^3 water, the mixing was completed in 20 minutes. [12] The paste was spread upon the grids with a spatula. Paper used to cover the plate after pasting took up some of the moisture. [12,13] As recommended by the manufacturer, [12] the complete drying of the plates before formation was accomplished at ordinary temperatures and humidities in 48 hours.

1.1.4.4 Formation of Pasted Plates: Formation, as applied to the Planté plates, means the creation of a layer of sponge lead on the surface of the negative plates and of lead peroxide on the positives to constitute the active materials of the cell. Formation of pasted plates, on the other hand, means the oxidation or reduction of the lead oxides and other materials which have been applied to the grids. [13]

The strength and amount of sulfuric acid used will depend upon the previous treatment of the plates. Usually, it is within the range 1.05 to 1.15 sp.gr. [13]

Formation undoubtedly starts in the region where the poorly conducting paste is in contact with the better conducting grid bars. Completion of formation is indicated by (1) the color of

the active materials, i.e., the plates have "cleared" and are uniform in color, and (2) the fact that the plates are gassing normally. [13]

The proper charging current will depend on the thickness and type of plates and on the temperature. The current is used more effectively at lower rates, and these are desirable for thin plates For plates in general, a current density of 2 to 5 mA/cm^2 is reasonable. The area is reckoned as the apparent surface of both sides of the plate. [13]

After formation is completed, it is advisable to pour out the electrolyte and replace it with acid of a strength that will finish at a specific gravity of 1.260 to 1.280 when the battery is fully charged. [13]

After drying for several days, the pasted plates (0.50 mm thick, 3.5 x 3.5 cm) were electrolytically formed in 50 ml sulfuric acid of 1.070 sp.gr. The model electrodes that are to become the positives are made the anode in the test cell and the plates for the negatives are made the cathode. The test cells were two-plate cells, with excess negative capacity. The plates and separator were allowed to absorb electrolyte before the charging began.

The formation was carried out in different steps with appropriate current densities. Starting with a current density of 4 mA/cm^2 in the first hour, the formation was continued for 50 hours at 1.5 to 2 mA/cm^2. Most of the time, when the conversion was 50% at the back side of the model electrode, the current density was reduced to 1 mA/cm^2 or lower, thus avoiding excessive

gassing.

1.1.4.5 Assembling Test Cells: The first test cell configuration for pasted model plates was a pyrex beaker with circular pasted plates (5 cm diameter) separated by a PVC ring and pressed together and onto the bottom of the horizontal cell. An improvement of the configuration was necessary because the reaction could not be prevented at the back side (bottom side) of the porous model electrode.

A rectangular test cell with a bottom plate made of plate glass (2 mm thick, 10 x 10 cm) and walls made of micro slides (1 mm thick, 1 x 3 inch) was sealed together with acid-resistant black wax. The thin pasted positive plate (0.5 mm thick, 35 x 35 mm) had already been tightly sealed to the supporting plate (see Sec. 1.1.4.4). The pasted negative plate is placed, with the rubber separator material, on top of the positive model electrode. Reflection from the positive of the two-plate sandwich construction was monitored during the formation of the plates by a Moseley chart recorder (model 680) connected to the Keithley electrometer (model 610C) and a silicon photocell (S1M--C). During the formation in 1.070 sp.gr. H_2SO_4, with a current density of 1.6 mA/cm^2 reckoned at one side, the back side could not be prevented from reacting so that the model electrode, because of gas evolution, came off the supporting glass plate, making the reflectance measuring impossible.

In the next test cell, the grid was completely sealed with wax on the supporting glass plate before pasting had begun. The excess black wax had been removed by scraping out the spacings

of the grid so the paste could be loaded into it. A pasted and cured positive plate, sealed on supporting glass, is shown in Figure 2 (see Sec. 1.1.5.1) from the detection side. The edges of the porous model electrode were sealed all around to the glass plate. Only active material between the grid spacings, contacting the grid, is supposed to react inward from the solution side and from the grid throughout the porous electrode towards the supporting glass plate.

Visual observations confirm this type of behavior. After about 7 hours, at a forming current density of 4 mA/cm^2 the color change has taken place at the edges of the grid spacings.

1.1.4.6 Measuring Reflectance: For these long-term experiments, two factors became critical, i.e., the stability of the light intensity and the stability of the light detector.

Instead of using a single D-C power supply (Heath IP - 12 battery eliminator) for the high intensity microscope lamp, a 6 volt car battery (Sears type 28A) has been employed in parallel with the power supply, thus eliminating the line fluctuations.

The Keithley high-impedance electrometer in connection with the silicon photocell showed serious fluctuations. Only by using a less sensitive scale could the fluctuations be reduced. Therefore, more specular reflections of the glass plate were allowed by changing the angle between illumination and detection and increasing the illuminated surface of the model electrode. This is, of

course, at the cost of less resolution of changes in reflectance.

In the early reflectance experiments, filter paper was used as standards of reflectance. In a previous report [1], it was reported that more than 5 filter papers were required to eliminate background interference. These results are in agreement with data obtained by Ingle, et al. [14] The filter paper experiments can also be used to check the suitability of the reflectance device by measuring the reflectance of the test cell relative to Whatman #1 filter paper.[15] Figure 3, (see Sec. 1.1.5.1) which shows cell reflectance as a function of the number of thicknesses of filter paper introduced into the cell, confirms the fact that 5 layers of paper were required to eliminate background interference. Two configurations are used, indicating that resolution decreases if another glass plate is introduced.

Barium sulfate pasted on supporting glass with the same thickness as the test cells is used as standard of reflectance for the second series of Planté experiments.

1.1.4.7 Planté Experiments (II): The difference in reflectance of the discharged and charged condition of the Planté lead plate has been investigated as a function of time.

In a separate cell, a circular Planté plate was charged and discharged. Every 5 minutes, the plate was taken out of the cell and placed in a reflectance cell with a thin layer of sulfuric acid. The difference in reflectance between the reflectance cell and a standard of reflectance ($BaSO_4$) was detected and measured with a silicon photocell connected to a

Keithley high-impedance electrometer and a Moseley chart recorder. The voltage of the light source was held constant at 6.00 V.

Figure 4 (see Sec. 1.1.5.1) shows the forming of a Planté plate in 1.07 sp.gr. H_2SO_4 during 50 minutes at a current density of 1 mA/cm^2 reckoned on one side of the plate, followed by (a) a 30 minute discharge at 0.5 mA/cm^2 and (b) a 20 minute discharge at a higher current density of 1 mA/cm^2. The difference in reflectance was a change of 6% between the discharged and charged conditions. The longer time required at 0.5 mA/cm^2 indicates that reflectance truly monitors the electrode reaction.

1.1.4.8 New Reflectance Device: The resolution can be improved by excluding the specular reflection of the glass plates. A new device of optical pyrex glass is in development with the following features:

(a) exclusion of specular reflection caused by the bottom glass by using matte black paint at the illumination side;

(b) exclusion of specular reflection caused by the supporting glass plate of the model electrode by using dibutyl phthalate (same refractive index as pyrex glass) between the two glass media;

(c) use of an operational amplifier with a "short-circuit" connection, resulting in a linear and stable response from the silicon photocell;

(d) change in illumination and viewing angle of the optical reflectance device, being more appropriate for the model electrode texture.

1.1.5 Appendices

1.1.5.1 Figures

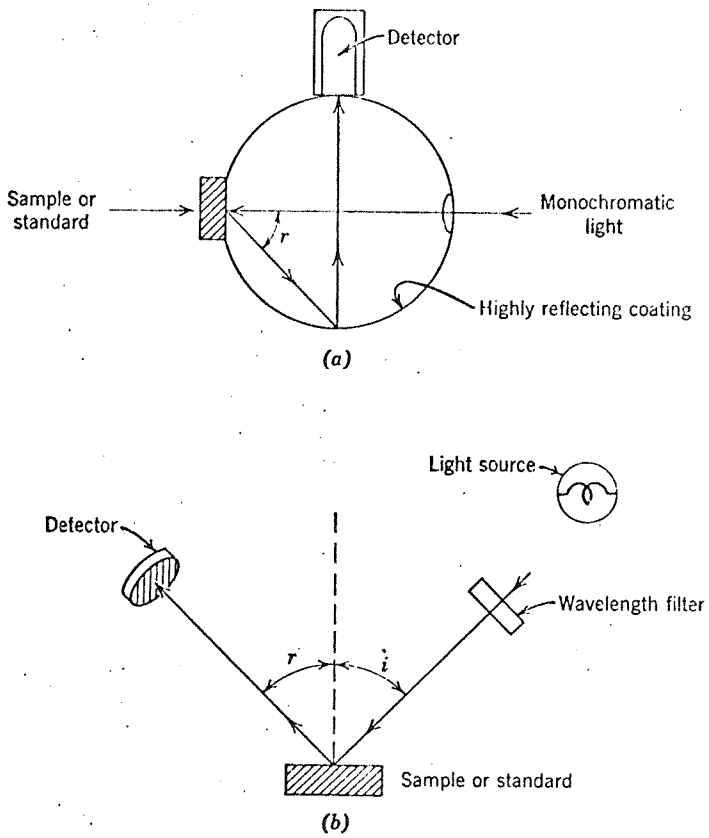

Fig. 1. Basic reflectance- or reflection-measuring instruments.
(a) Integrating sphere type.
(b) Reflection type.

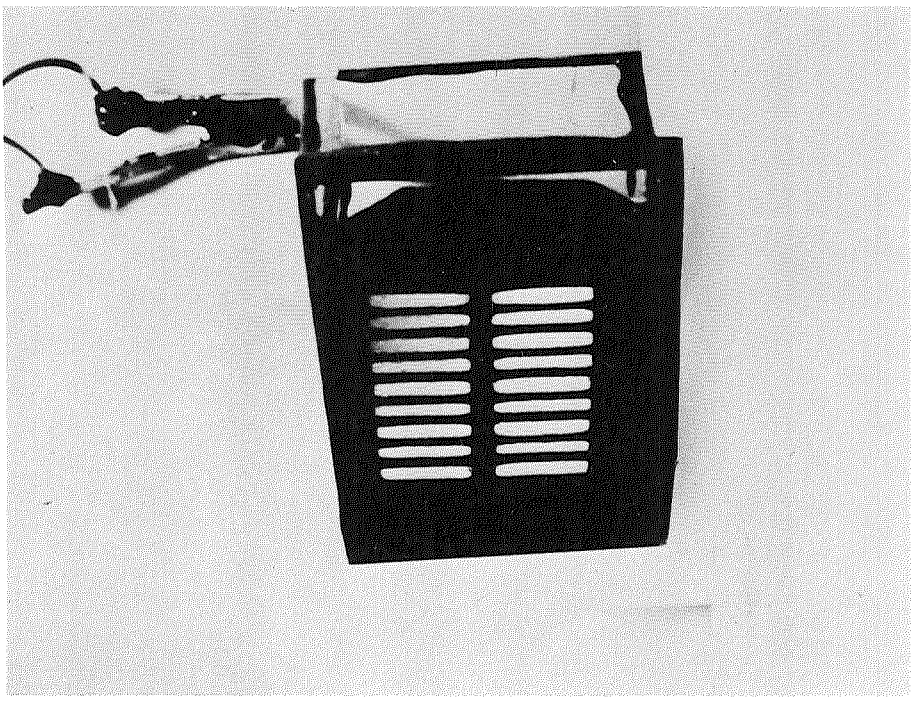

Fig. 2. A lead-acid test cell with a pasted and cured positive, sealed on supporting glass, viewed from the detection side.

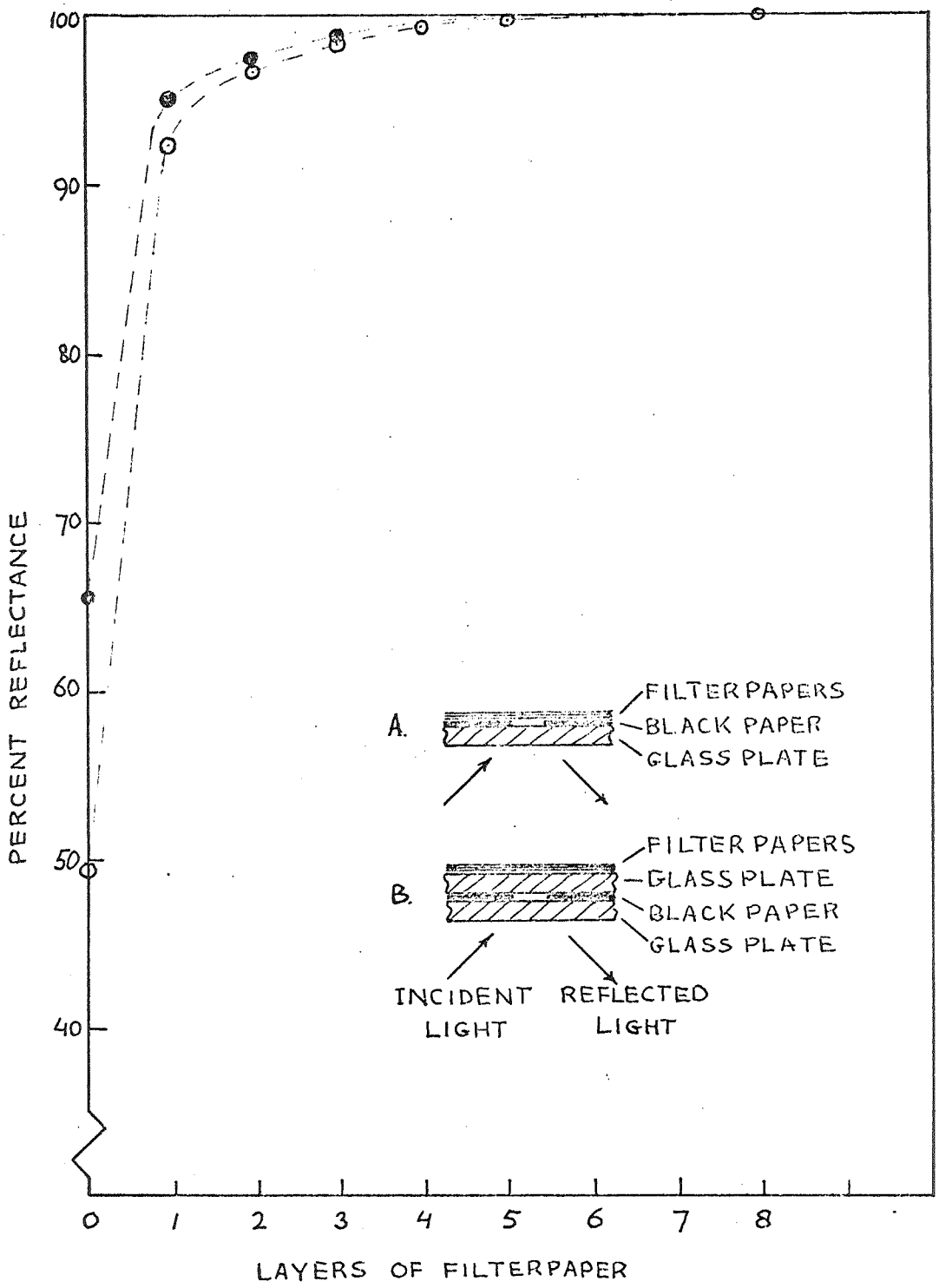

Fig. 3. Reflectance as a function of the number of thicknesses of filterpaper introduced onto two arrangements (A: ⊙ and B: ◉) of the reflectance device.

FIG. 4 REFLECTANCE OF POSITIVE PLANTÉ PLATES IN 1.07 sp.gr. H_2SO_4
(with $BaSO_4$ as standard of reflectance)

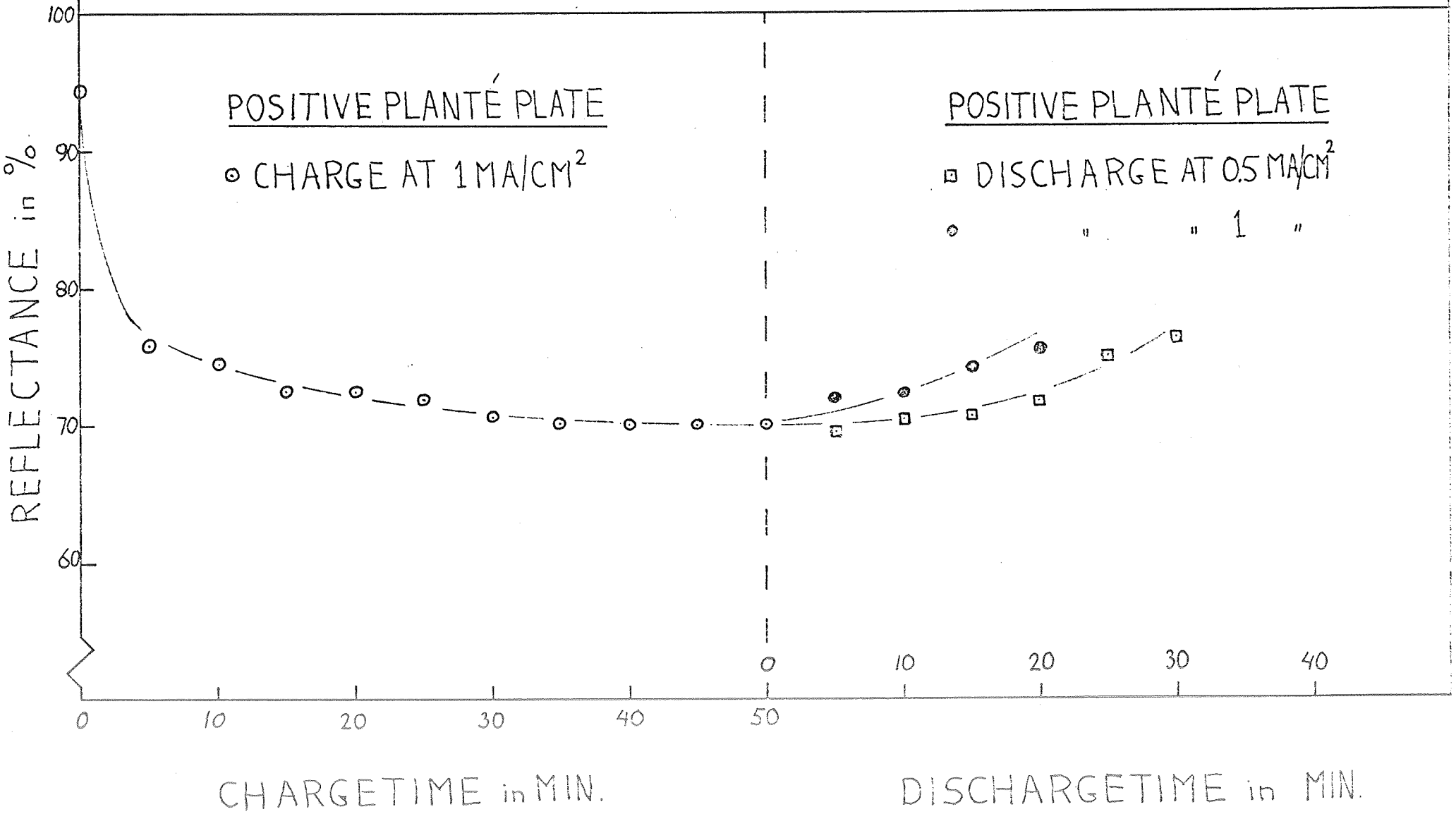

1.1.5.2 References

(1) School of Chemical Engineering, University of Pennsylvania, Contract No. 952-543 for JPL (Quart. Report Oct-Dec 1970, Jan-March 1971).

(2) G. Kortüm, "Reflectance Spectroscopy," Springer Verlag, New York (1969).

(3) F. W. Billmeyer, Jr. and R. T. Marcus, Appl. Optics 8, 763 (1969).

(4) W. W. Wendlandt and H. G. Hecht, "Reflectance Spectroscopy," Interscience Publ., New York (1966).

(5) F. W. Billmeyer, Jr., Appl. Optics 8, 737 (1969).

(6) F. Grum and G. W. Luckey, Appl. Optics 7, 2289 (1968).

(7) R. D. Grotti and L. D. Major, Texas Instruments, Bulletin CA-157 (Sept 1970).

(8) J. J. Loferski and J. J. Wysocki, RCA Rev. 22, 38 (1961).

(9) M. M. Koltun and T. M. Golovner, Opt. Spektrosk. 21, 630 (1966).

(10) P. G. Witherell and M. E. Faulhaber, Appl. Optics 9, 73 (1970).

(11) A. C. Simon, C. P. Wales and S. M. Caulder, J. Electrochem. Soc. 117, 987 (1970).

(12) Private Communication, J. Nees, National Lead Company.

(13) G. W. Vinal, "Storage Batteries," Wiley, New York (1955).

(14) R. B. Ingle and E. Minshall, J. Chromatog. 8,369 (1962).

(15) R. W. Frei and M. M. Frodyma, Anal. Chim. Acta 32,501 (1965).

1.2 Silver Oxide Electrode

1.2.1 Introduction

In a previous report [1], leaching experiments were described where anodically grown silver peroxynitrate crystals were converted to AgO. The purpose of this study was to synthesize crystals of AgO of sufficient size as to permit fabrication of a defined area electrode for further studies related to battery behavior (oxygen evolution, reduction to Ag_2O, etc.). Difficulties expected in conventional crystal-growing methods and encountered in a sophisticated pressurized-melt approach have been cited by Butler. [2] The leading step has been determined [3] as yielding a product whose X-ray diffraction pattern consists solely of AgO and traces of the starting material, $Ag_7O_8 \cdot NO_3$. [3]

In order to utilize the crystals of AgO produced by the leaching operation, it is necessary to determine whether a true crystal remains. B.E.T. surface area measurements were thus conducted on initial $Ag_7O_8 \cdot NO_3$ and leached crystals. As noted in a previous report [4], unusually low overvoltage was noted for oxygen evolution on an AgO crystal. An exchange current density (for a 4 electron oxidation of water to oxygen in alkaline solution) may be estimated from a linear fit of the sparse current-overvoltage data near the reversible potential. The calculated value of 1.2×10^{-3} Acm^{-2} is considerably greater than the range 10^{-6} to 10^{-4} Acm^{-2} reported in a recent review. [5]

1.2.2 B.E.T. Area Determination

Silver peroxynitrate crystals were freshly grown and large individual crystals were selected to provide lots of 1 gm each. The leaching was performed by immersing replicate samples of the crystals in boiling distilled water for one hour and also for eight days in distilled water at room temperature. B.E.T. studies were made by Micromeritics Instrument Corp., Norcross, Georgia. Table I summarizes the results obtained.

Table I

B.E.T. Surface Area
Treated Silver Peroxynitrate

No.	Condition	B.E.T. method	Surface Area, m^2/gm
1	As grown	Krypton, outgas, 25°C 900 min. adsorption	0.144
2	0.5 hr, 100°C; rinse; 0.5 hr, 100°C	" "	0.257
3	1 hr, 100°C	" "	0.539
4	8 day, 25°C	" "	0.487
5	As grown	Nitrogen, outgas, 100°C 40 min. adsorption	1.38

For samples 1 to 4, unusually long (900 min.) times were needed to equilibrate the surface with the B E.T. gas. Krypton was used principally because of the limited sample size.

1.2.3 Discussion

The as grown crystals were typically needle shaped,

1 cm long, with roughly square cross-section, .1 cm x .1 cm. From the known density of $Ag_7O_8 \cdot NO_3$ of about 6 gm cm^{-3}, the surface-to-volume ratio of the as-grown crystal should be very small, on the order of 0.0007 m^2/gm. Larger prismatic crystals were also included in sample No. 1. Thus, the most surprising aspect of the B.E.T. study is the very large, 0.144 m^2/gm, surface area found for the as-grown crystal. Leaching is seen to increase the surface area. For B.E.T. samples outgassed with heating at 100°C, a large change in area (to 1.38 m^2/gm) occurs because of the decomposition at 110°C. [3] As already noted in a previous report [1], a crystal of $Ag_7O_8 \cdot NO_3$ originally weighing 0.1323 gm or 98 x 10^{-5} mol Ag lost 15.6 x 10^{-5} mol Ag in the first 0.5 hr leach at 100°C, followed by a loss of 4 x 10^{-5} in the second 0.5 hr leach. After a loss of 1.2 x 10^{-5} mol Ag in the third leach, a total of 21% of the silver had been removed in 1.5 hr. This reaction rate is very great for a solid substance at 100°C, i.e., when compared with oxidation or corrosion rates. The initial substance was a single crystal of $Ag_7O_8 \cdot NO_3$ approximately 2 cm long and 0.1 cm x 0.1 cm square. Thus, a loss of 14.3% is expected if the Ag associated with the nitrate ion is leached completely from the crystal, in fair agreement with the actually found 21%. However, the large reaction rate implies some type of micro channel structure for the $Ag_7O_8 \cdot NO_3$ crystal.

The slow equilibration of the krypton used in the B.E.T. study also hints at microporosity. The B.E.T. equivalent particle size, which is roughly one thousand times smaller than

the actual crystal, also suggests an internal porosity and not a surface roughness effect. Silver peroxynitrate is considered as a cage clathrate structure with an open crystal lattice, but such internal area would even be orders of magnitude greater than the 0.1 m^2/gm level. Clearly, further work is needed to resolve this unusual behavior and whether the AgO produced by leaching of silver peroxynitrate may be used for defined area electrode studies or possibly for active battery positive material.

1.2.4 References

(1) Quarterly Report, Oct-Dec 1969, Sec. 1.1.6, JPL 952-543.

(2) Eliot A. Butler and Angus V. Blackham, 9th Quarterly JPL Report, 15 Aug 1970, Brigham Young University, Provo, Utah.

(3) Quarterly Report, Jan-March, April-June 1970, Sec. 1.1.1, JPL 952-543.

(4) Quarterly Report, Jan-March, April-June 1970, Sec. 1.1.2, JPL 952-543.

(5) G. D. Nagy and E. J. Casey, "Electrochemical Kinetics of Silver Oxide Electrodes," in Zinc-Silver Oxide Batteries, ed. A. Fleischer and J. J. Lander, Wiley, New York (1971).

2. Mass Transport

2.1 Membrane Permeation

2.1.1 Experimental

The rotating membrane apparatus described in previous reports was used to determine the permeation of zincate ion (in 40% KOH) at various temperatures and for various concentration differences. A 100 ml dose of 0.8M ZnO/40% KOH solution was introduced into the first compartment at zero time instead of 50 ml of 0.4M ZnO used previously, so that a larger step change of zinc concentration could be detected using atomic absorption methods. The time required to inject 100 ml of solution into the first compartment was about 20 seconds. For a given concentration in the first compartment, permeation proceeded for 30 minutes. Samples were taken from the second compartment at 2 minute intervals (started from zero time) in the first 6 minutes and then at intervals of 5 minutes for the rest of the run. Samples (1 ml) were also taken from the first compartment from which the step change of concentration can be determined. For each temperature, permeabilities were examined for three different zinc concentrations in a single run by using the impulse response technique as described in the previous report [9] as far as no leakage had occurred and the temperature control was within $\pm 0.5^{o}C$. A Keithley digital multimeter was used to record the output of a chromel-alumel thermocouple which was installed close to the membrane.

2.1.2 Results

Permeabilities of zinc through an acrylic-acid grafted, divinylbenzene cross-linked polyethylene membrane have been examined at temperatures of 11°C, 17°C, 21.5°C and 27°C. Figures 1, 2, 3 and 4 (see Sec. 2.1.6.1) give the concentration of zinc in the second and first compartments during a run using the step response technique. Figures 1 and 3 show only a part of a complete run, due to the occurrence of a leakage for the 11°C run and to the failure of cooling-water pump for the 27°C case. For the 17°C and 21.5°C runs, data for three different concentrations were obtained. Discontinuity in slope of the second (exit) compartment concentration vs. time corresponds to a step increase in zinc concentration in the first (input) compartment. The Zn concentration change in the first compartment ranges from 2.45×10^4 to 3.75×10^4 µg/ml and the concentration in the second compartment changes from 2.54 to 62 µg/ml in a 1.5 hour run. The range of fluctuation of the readings from the AA-120 atomic absorption spectrophotometer is also shown in the figures. Figures 5, 6, 7 and 8 are plots of

$$-\ln \left[1 + \frac{(C_{20}-C_2)(1 + V_2/V_1)}{C_{10} - C_{20}} \right] \quad \text{vs.} \quad (t - t_o)$$

as suggested by the analysis in the previous report [Ref. 9, Sec. 2.1.1.2]. The straight line fitting to the data points was made by least squares analysis. The correlation factors for all straight lines are greater than 0.995, which shows

the excellent fitting of the data by a straight line. From the slope of these straight lines, the overall permeation coefficient through the membrane and the boundary layers immediately adjacent to the membrane can be calculated. The results are tabulated in Table I. The permeation coefficients increase with the temperature but do not vary much with the concentration for a given temperature. No definite effect of the concentration on the permeation coefficient can be seen. The coefficients at 17°C and 21.5°C decrease with the concentration first and then increase, but the coefficient at 27°C increases with concentration. These deviations may be due to experimental error. An average value is appropriate to represent the permeation coefficient at any particular temperature.

2.1.3 Measurement of Membrane Thickness

Since the mass transfer coefficient of the membrane is the product of the permeation coefficient and the membrane thickness, a technique utilizing a microscope was developed to investigate precisely the thickness of a wet, swollen membrane without actual contact. The membrane was soaked in 40% KOH, 0.2M ZnO/40% KOH, 0.4M ZnO/40% KOH and 0.6M ZnO/40% KOH at 25°C respectively for at least one day before its thickness was measured. A piece of optically flat glass marked with black ink on both sides was used to calibrate the microscope height measurement. By focusing the microscope on the bottom and top surfaces of the glass plate, the scale reading on the height adjusting knob of the microscope corresponding to the thickness of the glass plate (measured by micrometer to 0.0001

Table I

Permeability Parameters, Polyethylene Separator

T, °C	$C_{10} \times 10^{-4}$, µg/ml	Slope of lines as shown in Figs. 5, 6, 7, 8 $\times 10^{7}$	$K \times 10^{5}$, cm/sec
11	2.45	-5.336	1.443
17	1.845	-8.151	2.204
17	2.793	-7.769	2.101
17	3.52	-8.284	2.24
21.5	1.868	-8.601	2.326
21.5	3.06	-8.046	2.176
21.5	3.75	-9.134	2.470
27	1.868	-9.973	2.697
27	3.06	-10.86	2.937

where

C_{10} = Concentration of zinc in the first compartment

K = Overall permeation coefficient

inch) was noted. To measure the thickness of the wet membrane, the microscope was focused on the top surface of the glass plate and on the top surface of the wet membrane placed on the glass plate. At a magnification of 262.5, ten scale divisions of the height knob corresponded to 0.001 inch. The dry membrane thickness was measured by micrometer to be 0.0011 inch. The thickness of the wet membrane was 0.00204 inch at 25°C, which was about 82% thicker than the dry membrane. The concentration of ZnO in 40% KOH did not produce any change in the thickness of the membrane. This result is helpful, since it implies that there will be no unequal expansion of a membrane which has a concentration gradient of zincate ion during active permeation in the apparatus. Investigation of the wet membrane thickness as a function of temperature is currently under way. By knowing the thickness at each temperature, the ion diffusivity in the membrane may be computed from the permeation coefficient (see Sec. 2.1.5). From the temperature dependence of the diffusion coefficient, it is possible to compute the energy of activation for the diffusion of zincate ion through the membrane for comparison with predictions of various transport models. These will be given in the next report.

2.1.4 Calculation of the Mass Transfer Coefficient in the Boundary Layer

The theoretical basis for the hydrodynamics of the rotating disc system is well known. The equations for the conservation of momentum and mass expressed in cylindrical coordinates are given by Schlichting [1]. Von Karman [2] (3)

introduced a similarity transformation which allows one to convert the partial differential equations to a set of ordinary differential equations. Gerad [4] used an analog computer to solve the set of equations with high Schmidt number and found the mass transfer correlation of Sherwood number and Reynolds number, Schmidt number, as

$$Sh = 0.62\ Re^{\frac{1}{2}}\ Sc^{\frac{1}{3}} \qquad \text{[Eqn. 1]}$$

where

$$Sh = \frac{K_b r}{D}, \qquad Re = \frac{r^2 w}{\nu}, \qquad Sc = \frac{\nu}{D}$$

K_b = mass transfer coefficient through the boundary layer

r = radius

D = diffusivity of the liquid

w = rotational speed

ν = kinematic viscosity

Smith [5], with a rotating membrane disc system similar to the present apparatus, investigated the well-studied dissolution of pressed benzoic acid in water. He confirmed the theoretical prediction (Eqn. 1) for the large tanks system with stirring but found that the coefficient should be 0.544 instead of 0.62 for small tanks. One may thus pre-calculate the mass transfer coefficient for the liquid through the boundary layer by knowing the rotating speed of the disc as well as the physical properties of the liquid.

The density and viscosity of a KOH--H_2O system at temperatures

of 25°C and 75°C have been reported by Klochko and Godneva [6]. Dirkse [7] has reported the density and viscosity of saturated solutions of ZnO in aqueous KOH at 25°C. Using the sparse data for the properties of ZnO/KOH-H_2O solutions, and assuming that the density and the viscosity vary linearly with the content of zinc in the aqueous KOH solution and, further, that they do not change very much in the temperature range of 11 to 27°C, it has been possible to apply Eqn. 1. A sample calculation of the mass transfer coefficient in the liquid is given in the Appendix (Sec. 2.1.6.1) for a rotating speed of 21.5 r.p.m. Since measurement of the diffusivity of zincate ion in 40% KOH solution is still underway, no exact value of diffusivity is available. However, a good approximation may be based on the value of 5.3×10^{-6} cm^2 sec^{-1} for the diffusivity of zincate ion in a 0.25M ZnO/23.4 wt% KOH solution found by Lu [8] [10] using a rotating disc electrode method. The value 5.1×10^{-6} cm^2/sec at 25°C is used for the present calculation of the mass transfer coefficient by adjusting Lu's result for the viscosity of the 40% KOH solution. Table II contains the results calculated for the coefficients through the boundary layer in the first compartment. The mass transfer coefficients in the second compartment do not vary because the concentration of zinc is so small that the transport properties of 40% KOH should be used. The value is given at the bottom of Table II.

2.1.5 Calculation of Membrane Mass Transfer Coefficient

The overall measured coefficient (see Table I) is related to the membrane permeability by the relation

$$\frac{1}{K} = \frac{1}{Km} + \frac{1}{K_{b1}} + \frac{1}{K_{b2}} \qquad \text{[Eqn. 2]}$$

if the equilibrium partition coefficient between the liquid interfacial concentration and the membrane interfacial concentration is assumed to be unity, i.e., $Cm = Cm^*$, where

Cm = Liquid concentration just at the membrane-liquid interface

Cm^* = Membrane concentration just at the membrane-liquid interface.

The permeation coefficient of the membrane can therefore be calculated from the measured overall permeation coefficient and the mass transfer coefficients through the boundary layers. The correction for the liquid boundary layers is a non-negligible 10%. Assuming the thickness of the wet membrane does not change within the temperature range of 11 to 27°C and using the value obtained at 25°C, the mass transfer coefficient, i.e., effective diffusivity, can therefore be calculated by multiplying the membrane permeation coefficient by the wet membrane thickness. The results are shown in Table III. Average values of the effective diffusion coefficients for each temperature are shown in the last column of Table III to be on the order of $10^{-7} cm^2\ sec^{-1}$. More refined calculation awaits determination of wet membrane thickness. Further improvement of the computation will also depend on yet to be determined free liquid diffusivity of zincate ion as a function of temperature and concentration. However, as a first approximation, the diffusivity of zincate ion in the membrane is less than the free liquid

Table II

Liquid Film Resistance Parameters

$T^{o}C$	$C_{10} \times 10^{-4}$ µg/ml	ρ g/cm^3	μ cp	$\left(\frac{r^2 \rho w}{\mu}\right)^{\frac{1}{2}}$	$\left(\frac{\mu}{\rho D}\right)^{\frac{1}{3}}$	$\frac{K_{b_1} r}{D}$	$K_{b_1} \times 10^4$ cm/sec
11	2.450	1.43	4.55	10.68	18.41	106.96	4.29
17	1.845	1.42	4.36	10.87	18.19	107.56	4.32
17	2.793	1.435	4.68	10.55	18.56	106.52	4.28
17	3.52	1.445	4.96	10.28	18.88	105.58	4.24
21.5	1.868	1.424	4.38	10.86	18.20	107.52	4.32
21.5	3.06	1.44	4.8	10.43	18.7	106.10	4.26
21.5	3.75	1.449	5.08	10.17	19.01	105.17	4.22
27	3.06	1.44	4.8	10.43	18.7	106.10	4.26
27	3.75	1.449	5.08	10.17	19.01	105.17	4.22
	C_{20} µg/ml					$\frac{K_{b_2} r}{D}$	$K_{b_2} \times 10^4$ cm/sec
	2.54 to 62	1.395	3.5	12.04	17.1	112.2	4.5

where

ρ = Density

μ = Viscosity

r = Radius of the rotating membrane

w = Angular velocity of the rotating membrane

D = Diffusivity of zinc in 40% KOH solution

K_{b_1} = Permeation coefficient of zinc through the boundary layer in the first compartment

K_{b_2} = Permeation coefficient of zinc through the boundary layer in the second compartment

diffusivity by a factor of about forty. On the basis of the data in Table III, the activation energy is roughly estimated as 6.6 Kcal per mol, in reasonable agreement with typical activation energies for aqueous ion diffusivity. Further hypotheses concerning models of membrane-ion interaction must await data for the membrane thickness and free liquid diffusivity of zincate vs. temperature.

Table III

Membrane Transport Parameters

T, °C	$C_{10} \times 10^{-4}$ µg/ml	$K \times 10^{5}$ cm/sec	$K_{b_1} \times 10^{4}$ cm/sec	$K_{b_2} \times 10^{4}$ cm/sec	$K_m \times 10^{5}$ cm/sec	D_m or $K_m L$ $cm^2/sec \times 10^{7}$	$D_{m_{ave}}$ $cm^2/sec \times 10^{7}$
11	2.45	1.443	4.29	4.5	1.544	0.800	0.8
17	1.845	2.204	4.32	4.5	2.449	1.270	
17	2.793	2.101	4.28	4.5	2.324	1.205	1.256
17	3.52	2.24	4.24	4.5	2.496	1.294	
21.5	1.868	2.326	4.32	4.5	2.600	1.348	
21.5	3.06	2.176	4.26	4.5	2.416	1.253	1.348
21.5	3.75	2.47	4.22	4.5	2.786	1.444	
27	1.868	2.697	4.32	4.5	3.073	1.593	1.676
27	3.06	2.937	4.26	4.5	3.392	1.759	

where

K_m = Permeation coefficient of zincate through membrane

D_m = Diffusion coefficient of zincate through membrane

2.1.6 Appendices

2.1.6.1 Sample Calculation of the Permeation Coefficient in the Liquid

The liquid permeation coefficient is calculated from Eqn. 2, Sec. 2.1.5 with coefficient 0.544 instead of 0.62.

$$Sh = 0.544\ Re^{\frac{1}{2}}\ Sc^{\frac{1}{3}} \qquad \text{[Eqn. 2, Sec. 2.1.5]}$$

or

$$\frac{K_b r}{D} = 0.544\left(\frac{r^2 w}{\nu}\right)^{\frac{1}{2}}\left(\frac{\nu}{D}\right)^{\frac{1}{3}}$$

$$w = 21.5 \times \frac{2\pi}{60} = 2.25 \text{ rad/sec}$$

To calculate the permeation coefficient of zinc through the boundary layer in the first compartment at temperature $17^{\circ}C$ and $C_{10} = 1.845 \times 10^4$ μg/ml, the density of the solution is assumed first and the wt% of Zn in 40% KOH aqueous solution is calculated.

Assume $\rho = 1.42\ g/cm^3$, then

$$X = \frac{1.845 \times 10^4}{1.42} \times 10^{-6} = 1.3\%$$

By checking the density of the solution at this wt% of Zn from available data and then calculating the wt% of Zn in the solution again, one can find the exact density of the solution. The viscosity of the solution can also be found after the wt% Zn in the solution is known. For the solution of $17^{\circ}C$ and

$C_{10} = 1.845 \times 10^4$ µg/ml, the density is 1.42 g/cm^3 and the viscosity is 4.36 cp.

Thus,

$$\left(\frac{\gamma^2 w\rho}{\mu}\right)^{\frac{1}{2}} = \left[\frac{\left(\frac{0.5}{12}\right)^2 \times 2.25 \times 1.42 \times 62.4}{4.36 \times 6.72 \times 10^{-4}}\right]^{\frac{1}{2}} = 10.87$$

$$\left(\frac{\mu}{\rho D}\right)^{\frac{1}{3}} = \left[\frac{4.36 \times 10^{-2}}{1.42 \times 5.1 \times 10^{-6}}\right]^{\frac{1}{3}} = 18.19$$

and

$$K_b = \frac{0.544 \times 10.87 \times 18.19 \times 5.1 \times 10^{-6}}{0.5 \times 2.54} = 4.32 \times 10^{-4} \text{ cm/sec}$$

2.1.6.2 Figures

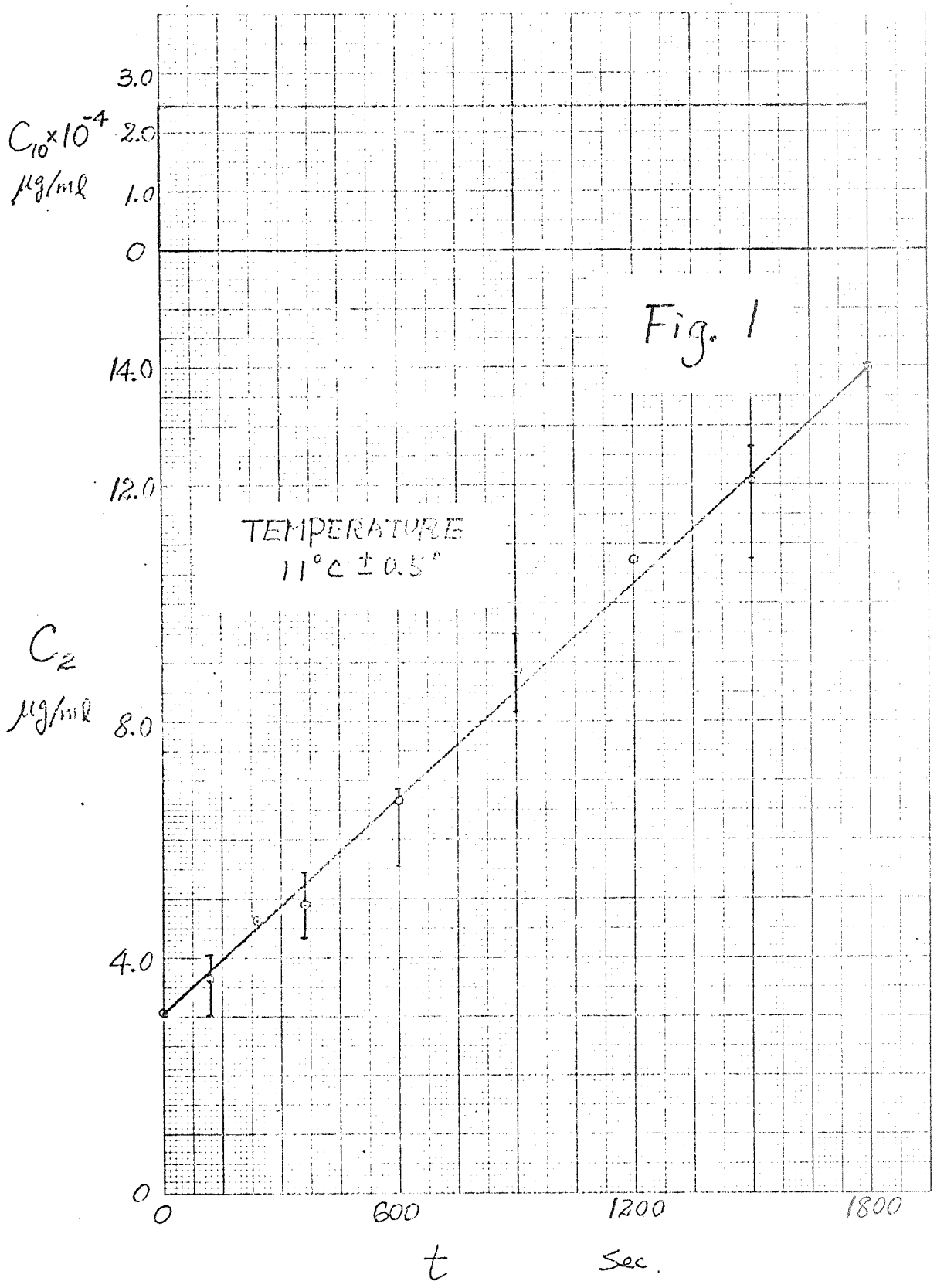

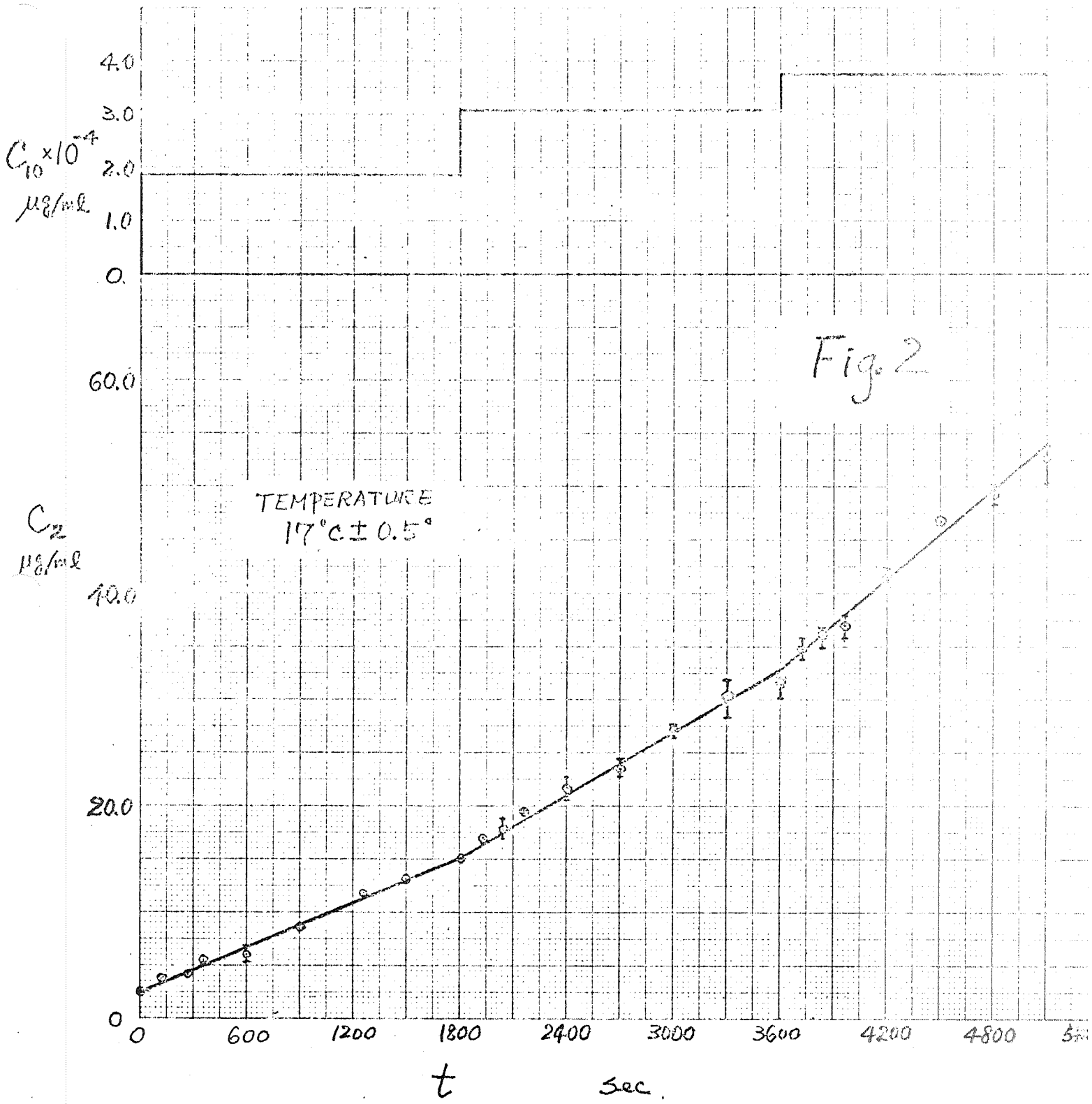
4.0
3.0
$C_{10} \times 10^{-7}$
μg/ml
2.0
1.0
0.
60.0
TEMPERATURE
17°C ± 0.5°
C_2
μg/ml
40.0
20.0
0
0
600
1200
1800
2400
3000
3600
4200
4800
t
sec.

Fig. 2

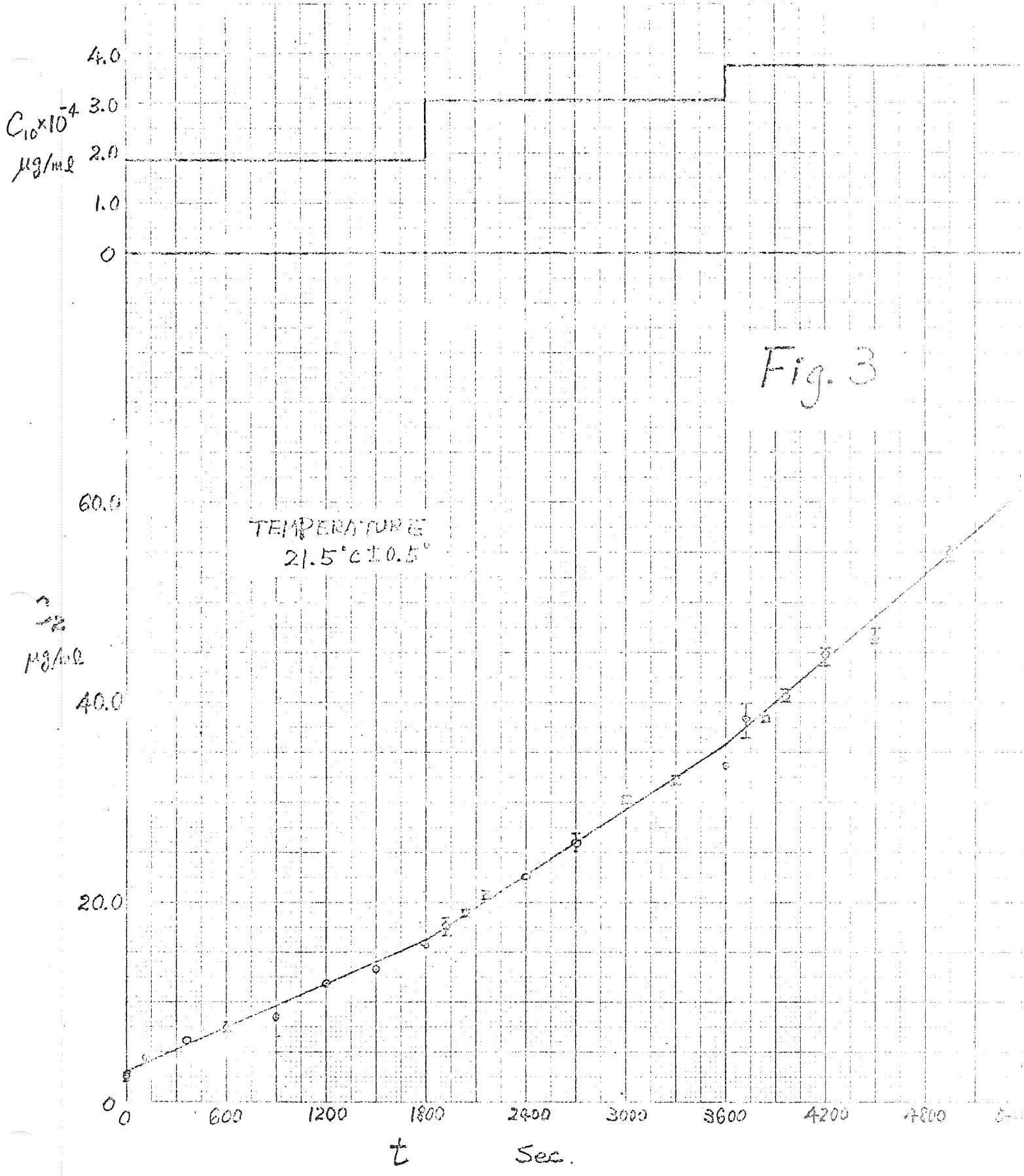
4.0
3.0
2.0
1.0
0
$C_{10} \times 10^{-4}$ μg/ml
60.0
40.0
20.0
0
μg/ml
TEMPERATURE
21.5°C ± 0.5°
0
600
1200
1800
2400
3000
3600
4200
4800
t Sec.

Fig. 3

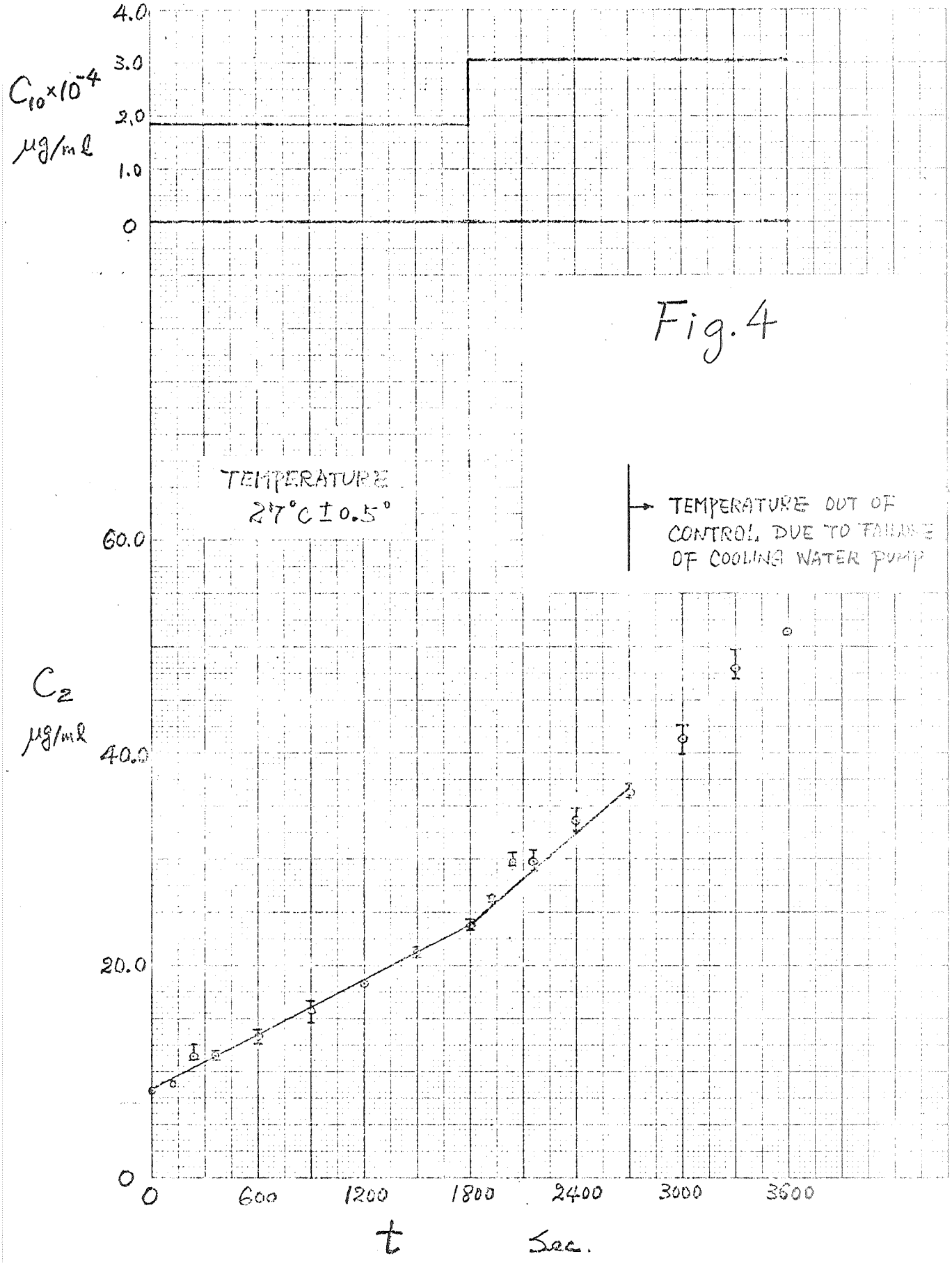
$C_{10} \times 10^{-4}$ μg/ml
4.0
3.0
2.0
1.0
0
TEMPERATURE 27°C ± 0.5°
TEMPERATURE OUT OF CONTROL DUE TO FAILURE OF COOLING WATER PUMP
C_2 μg/ml
60.0
40.0
20.0
0
0
600
1200
1800
2400
3000
3600
t Sec.

Fig. 4

$$-\ln\left[1+\frac{(C_{10}-C_2)(1+V_2/V_1)}{C_{10}-C_{20}}\right] \times 10^4$$

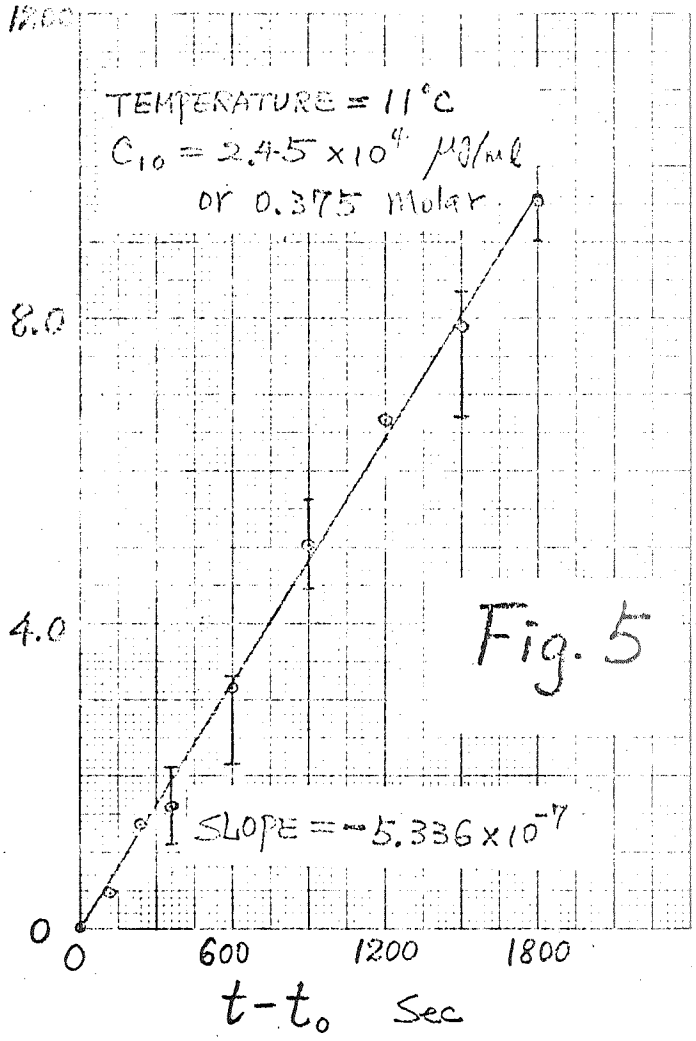

Fig. 5

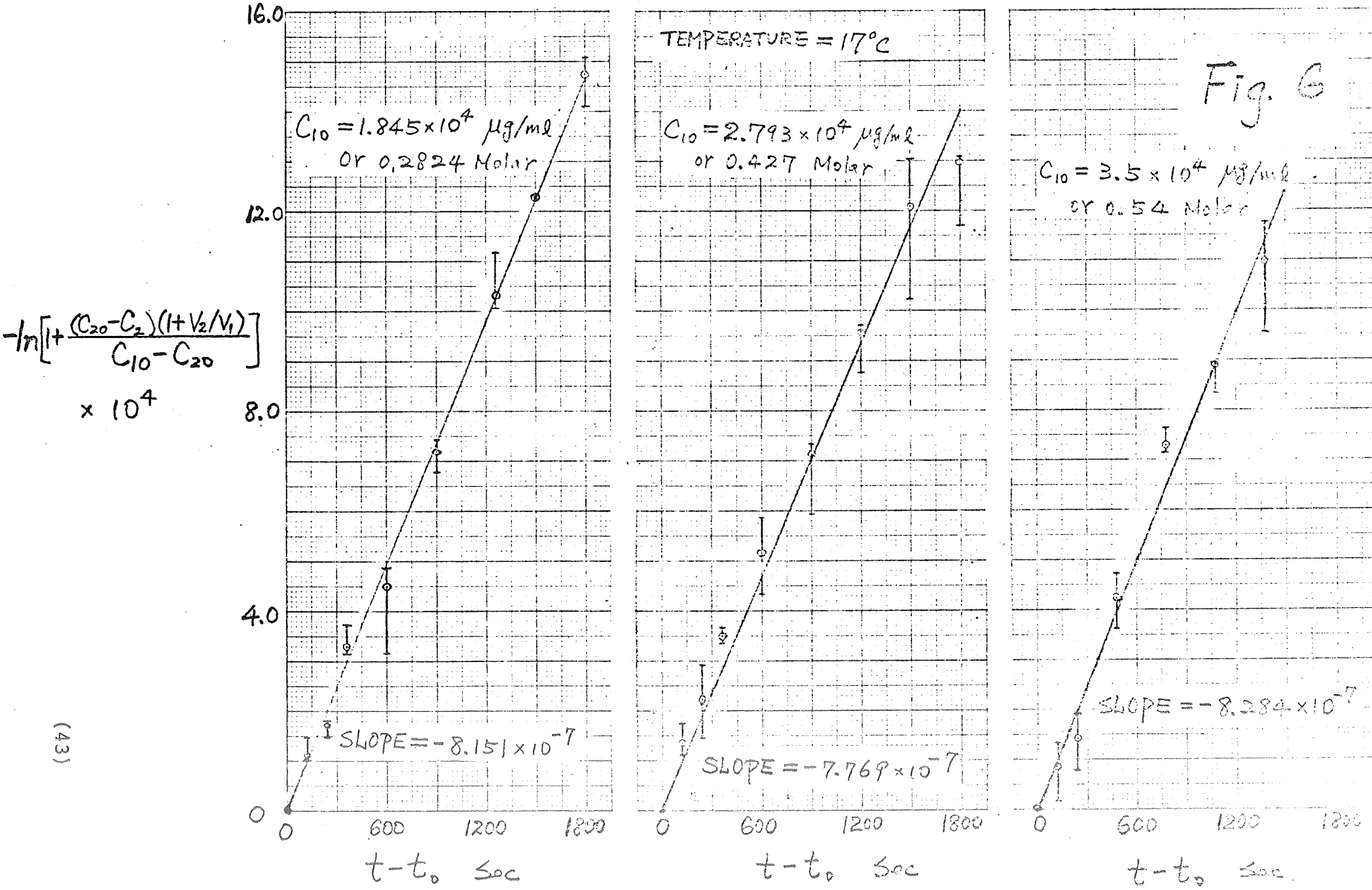
$-\ln\left[1+\frac{(C_{20}-C_2)(1+V_2/V_1)}{C_{10}-C_{20}}\right] \times 10^4$
16.0
12.0
8.0
4.0
0
0
600
1200
1800
$t-t_0$ Sec
$C_{10} = 1.845 \times 10^4$ µg/ml
or 0.2824 Molar
SLOPE $= -8.151 \times 10^{-7}$
TEMPERATURE = 17°C
$C_{10} = 2.793 \times 10^4$ µg/ml
or 0.427 Molar
SLOPE $= -7.769 \times 10^{-7}$
$C_{10} = 3.5 \times 10^4$ µg/ml
or 0.54 Molar
SLOPE $= -8.284 \times 10^{-7}$

Fig. 6

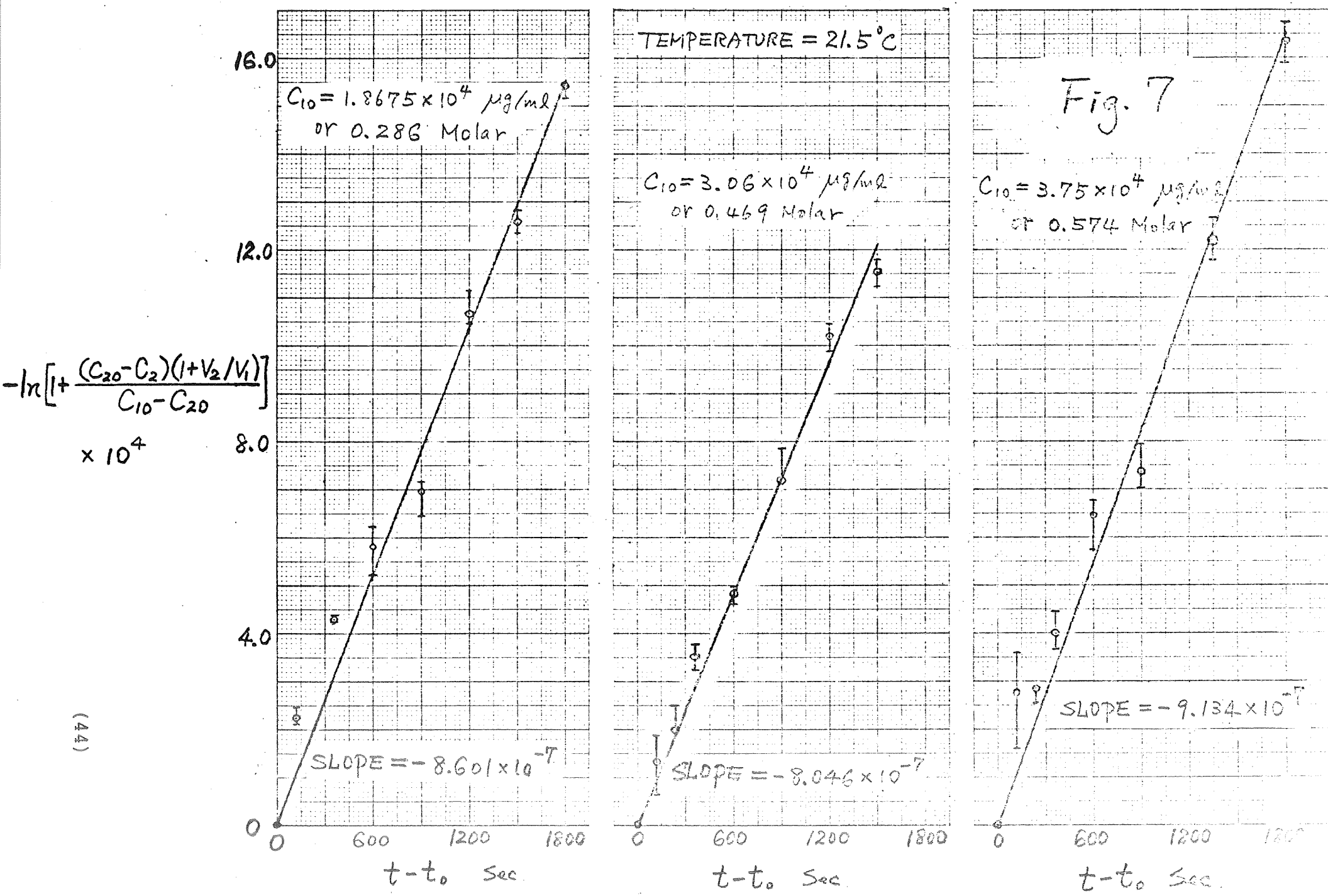
TEMPERATURE = 21.5°C
Fig. 7
$C_{10} = 1.8675 \times 10^4$ µg/ml
or 0.286 Molar
$C_{10} = 3.06 \times 10^4$ µg/ml
or 0.469 Molar
$C_{10} = 3.75 \times 10^4$ µg/ml
or 0.574 Molar
$-\ln\left[1+\frac{(C_{20}-C_2)(1+V_2/V_1)}{C_{10}-C_{20}}\right] \times 10^4$
16.0
12.0
8.0
4.0
0
0
600
1200
1800
$t-t_0$ Sec
SLOPE $= -8.601 \times 10^{-7}$
SLOPE $= -8.046 \times 10^{-7}$
SLOPE $= -9.134 \times 10^{-7}$

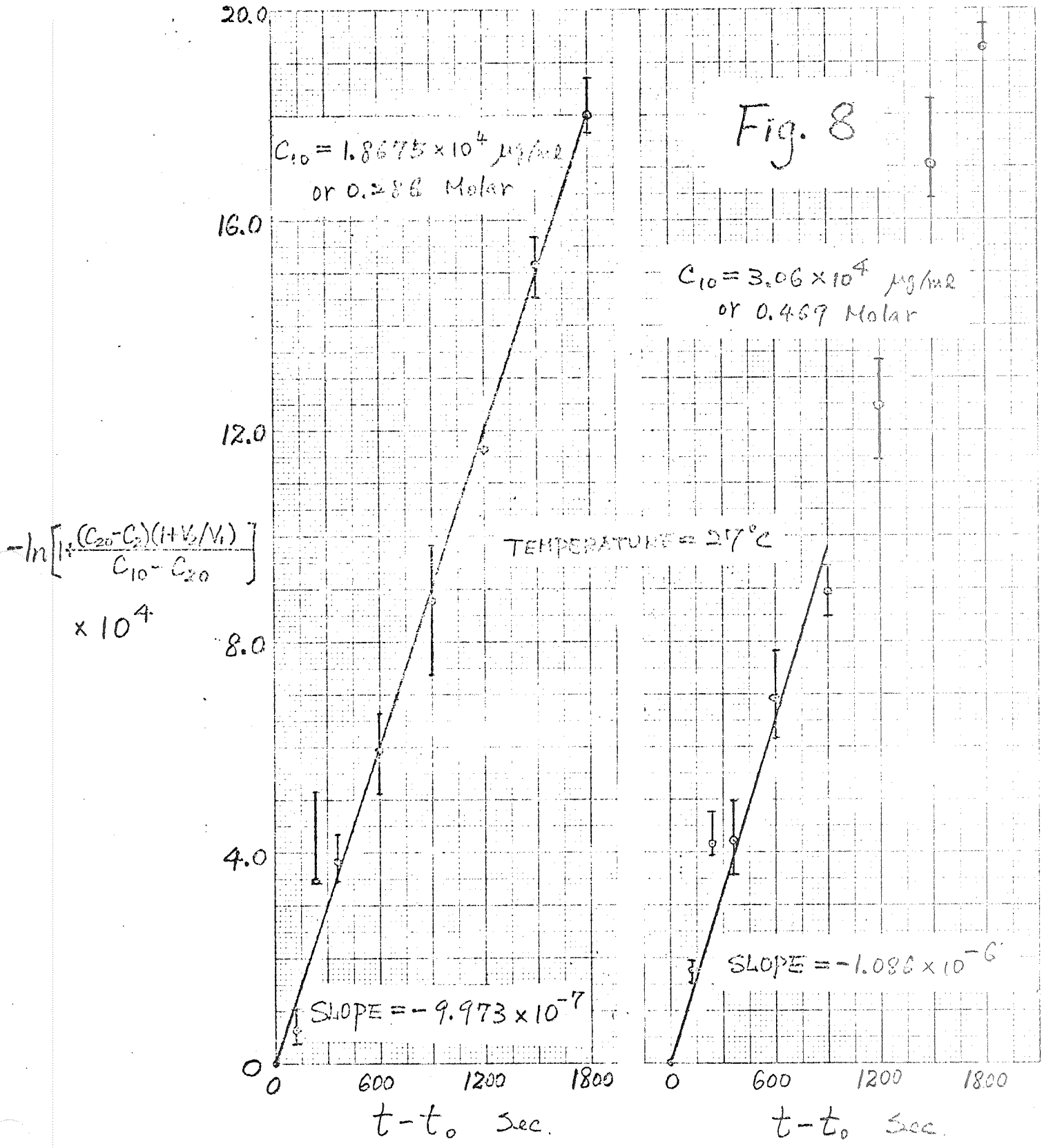
Fig. 8
$C_{10} = 1.8675 \times 10^{-4}$ μg/ml
or 0.288 Molar
$C_{10} = 3.06 \times 10^{-4}$ μg/ml
or 0.469 Molar
TEMPERATURE = 27°C
$-\ln\left[1+\frac{(C_{20}-C_2)(1+V_2/V_1)}{C_{10}-C_{20}}\right] \times 10^4$
20.0
16.0
12.0
8.0
4.0
0
0
600
1200
1800
SLOPE = -9.973×10^{-7}
SLOPE = -1.088×10^{-6}
$t - t_0$ Sec.
$t - t_0$ Sec.

2.1.6.3 References

(1) H. Schlichting, Boundary Layer Theory, 4th ed., McGraw-Hill Publ. Co., New York (1960).

(2) T. Von Karman, Z. Angew. Math. Mech. 1, 233 (1921).

(3) T. Von Karman, Z. Angew. Math. Mech. 1, 245 (1921).

(4) G. Serad, M.S. Thesis, Chem. Eng. Dept., University of Pennsylvania (1962).

(5) W. Smith, Ph.D. Thesis, University of Pennsylvania (1968).

(6) M. Klochko and M. Godneva, Russ. J. Inorg. Chem. 4, 964 (1959).

(7) T. Dirkse, J. Electrochem. Soc. 106, 154 (1959).

(8) C. Lu, M.S. Thesis, Chem. Eng. Dept., University of Pennsylvania (1970).

(9) Quarterly Report, Oct-Dec 1970, Jan-March 1971, JPL 952-543.

(10) Quarterly Report, July-Sept 1970, Sec. 1.2, JPL 952-543.

2.2 Capillary Diffusivity Model

2.2.1 Mathematical Model

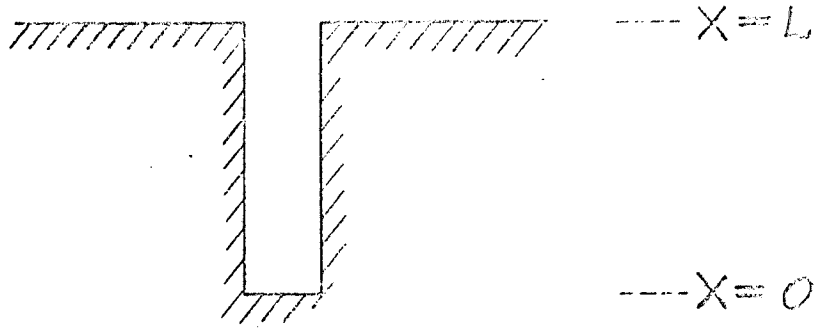

Fig. 9

The diffusion of electrolyte from a capillary to an external bulk solution as shown in Figure 9 is governed by the following differential equations:

(1) In the region $0 \leq X < L$, the diffusion is assumed to be one dimensional, so

$$\frac{\partial C}{\partial t} = D \frac{\partial^2 C}{\partial X^2} \qquad \text{[Eqn. 1]}$$

The boundary condition is

$$\frac{\partial C}{\partial X} = 0 \quad \text{at } X = 0,\ t \geq 0 \qquad \text{[Eqn. 2]}$$

The initial condition is

$$C = C_o \quad \text{at } 0 \leq X \leq L,\ t = 0 \qquad \text{[Eqn. 3]}$$

(2) In the region X > L, the diffusion may be three dimensional for no flow beyond X = L, or one dimensional for flow sufficient to maintain a zero concentration at X = L. Only the three dimensional diffusion model will be considered. The three dimensional version of Ficks second law (the diffusion equation) is

$$\frac{\partial c}{\partial t} = D\left(\frac{\partial^2 c}{\partial x^2} + \frac{\partial^2 c}{\partial y^2} + \frac{\partial^2 c}{\partial x^2}\right) \qquad \text{[Eqn. 4]}$$

The boundary condition for the three dimensional region beyond the capillary mouth at X = L is

$$c = 0 \quad \text{as } x \to \infty,\ y \to \infty,\ z \to \infty \text{ and } t \geq 0. \qquad \text{[Eqn. 5]}$$

The initial condition is

$$c = 0 \quad \text{as } x > L \text{ and } t = 0, \qquad \text{[Eqn. 6]}$$

corresponding to a region initially free of diffusant.

(3) At the junction between one and three dimensional regions at the mouth of the capillary (X = L), equality of fluxes gives

$$\left(\frac{\partial c}{\partial x}\right)_1 = \left(\frac{\partial c}{\partial x}\right)_3 + \left(\frac{\partial c}{\partial y}\right)_3 + \left(\frac{\partial c}{\partial z}\right)_3 \qquad \text{[Eqn. 7]}$$

The subscripts 1 and 3 indicate one dimensional and three dimensional regions respectively.

Equations 1 to 7 may be written in non-dimensional form by defining the following parameters:

$$\phi = \frac{c}{c_o}, \quad \eta = \frac{x}{L}, \quad \xi = \frac{y}{L}, \quad \beta = \frac{z}{L}, \quad \tau = \frac{Dt}{L^2}$$

where

c = concentration of diffusant

c_o = initial concentration of diffusant inside the capillary

L = length of the capillary

D = diffusivity of diffusant

t = time

Then, in the region $0 \leq \eta < 1$ where one dimensional diffusion exists,

$$\frac{\partial \phi}{\partial \tau} = \frac{\partial^2 \phi}{\partial \eta^2} \qquad \text{[Eqn. 8]}$$

The zero flux boundary condition at the closed end ($X = 0$) of the capillary becomes

$$\frac{\partial \phi}{\partial \eta} = 0 \qquad \text{at } \eta = 0 \text{ and } \tau > 0 \qquad \text{[Eqn. 9]}$$

The initial condition is

$$\phi = 1 \qquad \text{at } 0 \leq \eta \leq 1 \text{ and } \tau = 0. \qquad \text{[Eqn. 10]}$$

In the region of three dimensional diffusion, $\eta > 1$.

$$\frac{\partial \phi}{\partial \tau} = \frac{\partial^2 \phi}{\partial \eta^2} + \frac{\partial^2 \phi}{\partial \xi^2} + \frac{\partial^2 \phi}{\partial \beta^2} \qquad \text{[Eqn. 11]}$$

The boundary condition in Eqn. 5 becomes

$$\phi = 0 \qquad \text{at } \eta \to \infty, \quad \xi \to \infty, \quad \beta = \infty, \text{ and } \tau \geq 0 \qquad \text{[Eqn. 12]}$$

Eqn. 7 becomes

$$\left(\frac{\partial \phi}{\partial \eta}\right)_1 = \left(\frac{\partial \phi}{\partial \eta}\right)_3 + \left(\frac{\partial \phi}{\partial \xi}\right)_3 + \left(\frac{\partial \phi}{\partial \beta}\right)_3 \qquad \text{[Eqn. 13]}$$

at $\eta = 1$, $\xi = 0$, $\beta = 0$ and $\tau \geq 0$

Eqn. 14 indicates symmetry of diffusion perpendicular to the axis of the capillary.

$$\frac{\partial \phi}{\partial \xi} = 0, \quad \frac{\partial \phi}{\partial \beta} = 0 \qquad \text{at } \xi = 0,\ \beta = 0,\ \tau \geq 0 \text{ and } \eta > 1. \qquad \text{[Eqn. 14]}$$

The initial condition of Eqn. 6 becomes

$$\phi = 0 \quad \text{as } \eta > 1,\ 0 \leq \xi \leq \infty,\ 0 \leq \beta \leq \infty, \text{ and } \tau = 0. \qquad \text{[Eqn. 15]}$$

2.2.2 Finite Difference Equations

An explicit form of the finite difference equation was used to represent the equations formulated in Sec. 2.2.1.[1]

In the one dimensional diffusion region, $0 \leq \eta \leq 1$, Eqn. 16 applies:

$$\phi_{i,1,1,n+1} = [1-2\lambda_1]\ \phi_{i,1,1,n} + \lambda_1\ [\phi_{i-1,1,1,n} + \phi_{i+1,1,1,n}]$$

$$\frac{1}{\Delta\eta} > i > 2. \qquad \text{[Eqn. 16]}$$

At $i = 1$,

$$\phi_{1,1,1,n+1} = [1-2\lambda_1]\ \phi_{1,1,1,n} + 2\lambda\phi_{2,1,1,n}. \qquad \text{[Eqn. 17]}$$

$$\phi_{i,1,1,0} = 1 \quad \text{(initial condition)} \qquad \text{[Eqn. 18]}$$

In the three dimensional diffusion region, $\eta > 1$, $0 \leq \xi \leq \infty$, $0 \leq \beta \leq \infty$, we have

$$\phi_{i,j,k,n+1} = (1-2\lambda_1 - 2\lambda_2 - 2\lambda_3)\ \phi_{i,j,k,n} + \lambda_1\ (\phi_{i-1,j,k,n} + \phi_{i+1,j,k,n}) + \lambda_2\ (\phi_{i,j-1,k,n} + \phi_{i,j+1,k,n}) + \lambda_3\ (\phi_{i,j,k-1,n} + \phi_{i,j,k+1,n}) \quad \text{for } i > \frac{1}{\Delta\eta}\ . \qquad \text{[Eqn. 19]}$$

Boundary conditions are:

$$\phi_{i,j,k,n} = 0 \quad \text{as } i \to \infty,\ j \to \infty,\ k \to \infty \qquad \text{[Eqn. 20]}$$

$$\phi_{i,o,k,n} = \phi_{i,2,k,n} \qquad \text{[Eqn. 21]}$$

$$\phi_{i,j,o,n} = \phi_{i,j,2,n} \qquad \text{[Eqn. 22]}$$

Initial condition is:

$$\phi_{i,j,k,n} = 0 \quad \text{as } \tau = 0,\ i > \frac{1}{\Delta\eta},\ 0 \le j \le \infty,\ 0 \le k \le \infty. \qquad \text{[Eqn. 23]}$$

Suppose λ_1, λ_2, λ_3 are chosen equal, then at the junction between one and three dimensional regions, i.e., $i = \frac{1}{\Delta\eta}$ or $i = M$, we have

$$\phi_{M,1,1,n+1} = \phi_{M,1,1,n} + \lambda[\phi_{M+1,2,2,n} - 2\phi_{M,1,1,n} + \phi_{M-1,1,1,n}] \qquad \text{[Eqn. 24]}$$

where:

i = index for the step movement in x direction

j = " " " " " " " y " "

k = " " " " " " " z " "

n = time

$\Delta\tau$ = step increment in time

$\Delta\eta$ = " " " " x direction

$\Delta\beta$ = " " " " y direction

$\Delta\xi$ = " " " " z direction

$M = \frac{1}{\Delta\eta}$: number of calculations in the capillary

$\lambda_1 = \frac{\Delta\tau}{(\Delta\eta)^2}$

$\lambda_2 = \frac{\Delta\tau}{(\Delta\beta)^2}$

$\lambda_3 = \frac{\Delta\tau}{(\Delta\xi)^2}$

Summary of the finite difference equations:

(1) $\phi_{1,1,1,n+1} = [1-2\lambda]\phi_{1,1,1,n} + 2\lambda\phi_{2,1,1,n}$ [Eqn. 17]

(2) $\phi_{i,1,1,n+1} = [1-2\lambda]\phi_{i,1,1,n} + \lambda[\phi_{i-1,1,1,n} + \phi_{i+1,1\ 1,n}]$

for $M > i \geq 2$ [Eqn. 25]

(3) $\phi_{M,1,1,n+1} = \phi_{M,1,1,n} + \lambda[\phi_{M+1,2,2,n} - 2\phi_{M,1,1,n} + \phi_{M-1,1,1,n}]$

[Eqn. 26]

(4) $\phi_{i,j,k,n+1} = (1-6\lambda)\phi_{i,j,k,n} + \lambda[\phi_{i-1,j,k,n} + \phi_{i+1,j,k,n} +$

$\phi_{i,j-1,k,n} + \phi_{i,j+1,k,n} + \phi_{i,j,k-1,n} + \phi_{i,j,k+1,n}]$

for $i > M$, $j \neq 1$, $k \neq 1$

[Eqn. 27]

$$(5)\quad \phi_{i,1,1,n+1} = (1-6\lambda)\phi_{i,1,1,n} + \lambda[\phi_{i-1,1,1,n} + \phi_{i+1,1,1,n} + 2\phi_{i,2,1,n} + 2\phi_{i,1,2,n}] \qquad \text{for } j = 1,\ k = 1 \qquad \text{[Eqn. 28]}$$

$$(6)\quad \phi_{i,1,k,n+1} = (1-6\lambda)\phi_{i,1,k,n} + \lambda[\phi_{i-1,1,k,n} + \phi_{i+1,1,k,n} + 2\phi_{i,2,k,n} + \phi_{i,1,k-1,n} + \phi_{i,1,k+1,n}] \qquad \text{for } j = 1,\ k \neq 1 \qquad \text{[Eqn. 29]}$$

$$(7)\quad \phi_{i,j,1,n+1} = (1-6\lambda)\phi_{i,j,1,n} + \lambda[\phi_{i-1,j,1,n} + \phi_{i+1,j,1,n} + \phi_{i,j-1,1,n} + \phi_{i,j+1,1,n} + 2\phi_{i,j,2,n}] \qquad \text{for } j \neq 1,\ k = 1 \qquad \text{[Eqn. 30]}$$

2.2.3 Results and Discussion

The above finite difference equations (Eqn. 17, 25-30) were solved on a digital computer to determine the residual amount of diffusant in the capillary as a function of time and diffusion coefficient. The finite difference equations for one dimensional and two dimensional diffusion from a virtual slot out into the stationary bulk solution were also solved on the computer. A numerical solution for the diffusion from the capillary with fluid flow over the mouth to maintain zero boundary condition was solved and compared to the analytical solution. The results are shown in Figure 10. The excellent agreement between the analytical and the numerical solutions for diffusion with zero boundary condition show the adequacy of the numerical scheme and its stability with the chosen step size. The same step size was

used throughout the computation. The curves for diffusion with stirring and for one dimensional diffusion without stirring became the lower and upper bounds for all solutions. In the short time region ($\tau < 0.5$), diffusion with stirring was about four times faster than that for one dimensional diffusion without stirring. The diffusion rate for three dimensional diffusion is about 1.6 times higher than for one dimensional diffusion in the short time region and about 2.9 times higher in the long time region. A plot of the dimensionless concentration profile in the capillary vs. distance as a function of dimensionless time for three dimensional diffusion without stirring and for diffusion with stirring is shown in Figure 11.

If stirring is not provided to sweep away the accumulated diffusant from the capillary mouth region, the amount remaining in the capillary may be analyzed and incorrectly used in the equation for zero boundary condition to calculate the diffusion coefficient. The apparent value of D so computed will clearly be less than the true value of the diffusion coefficient. The negative deviations arising from misapplication of Eqn. 6, Sec. 2.3.5 is shown in Table IV as a function of the amount of electrolyte remaining in the capillary. If sufficient time is allotted, even without stirring past the mouth of the capillary, the diffusant must ultimately diminish the initial amount in the capillary and, after a very long time, it might be suspected that there will exist some convergence of the two extreme cases provided by stirring and no stirring. Table IV shows the tendency of this approach. A plot of Dapp/Dact vs. Cave/Co is given in Figure 12. The ratio of the apparent

diffusion coefficient to the actual diffusion coefficient increases toward unity as the remaining material in the capillary decreases. However, the time required for this convergence is so long that little material remains in the capillary. Thus, a precise prediction of the diffusion coefficient from the measured amount of electrolyte remaining in the capillary for non-stirring diffusion is absolutely necessary and an extremely useful advance in the capillary method. With the results tabulated in Table IV, it is possible to back-correct data in the literature where Eqn. 6, Sec. 2.3.5 has been used incorrectly with no-stirring. Also, an entirely novel and simplified experimental technique may be designed which totally eliminates the ambiguity associated with stirring and the $\Delta\ell$-effect. A capillary with a slight temperature gradient (cold bottom) will be necessary to prevent thermally-induced convection for the non-stirred arrangement.

Table IV

C_{ave}/C_o	D_{app} t/L^2 *	D_{act} t/L^2	D_{app}/D_{act}
0.9202	0.0050	0.0195	0.256
0.887	0.0100	0.0300	0.333
0.85	0.0177	0.0438	0.404
0.8	0.0311	0.0655	0.475
0.75	0.0482	0.0915	0.527
0.7	0.0700	0.1210	0.579
0.65	0.0955	0.1540	0.620
0.6	0.1250	0.1910	0.655
0.55	0.1580	0.2340	0.675
0.5	0.1950	0.2800	0.700
0.45	0.2380	0.3310	0.719
0.4	0.2840	0.3870	0.734
0.35	0.3400	0.4530	0.751
0.3	0.4010	0.5280	0.760
0.25	0.4740	0.6170	0.768
0.2	0.5620	0.7260	0.774
0.15	0.6740	0.8670	0.777
0.113	0.80	1.0	0.800

* Based on Eqn. 6, Sec. 2.3.5.

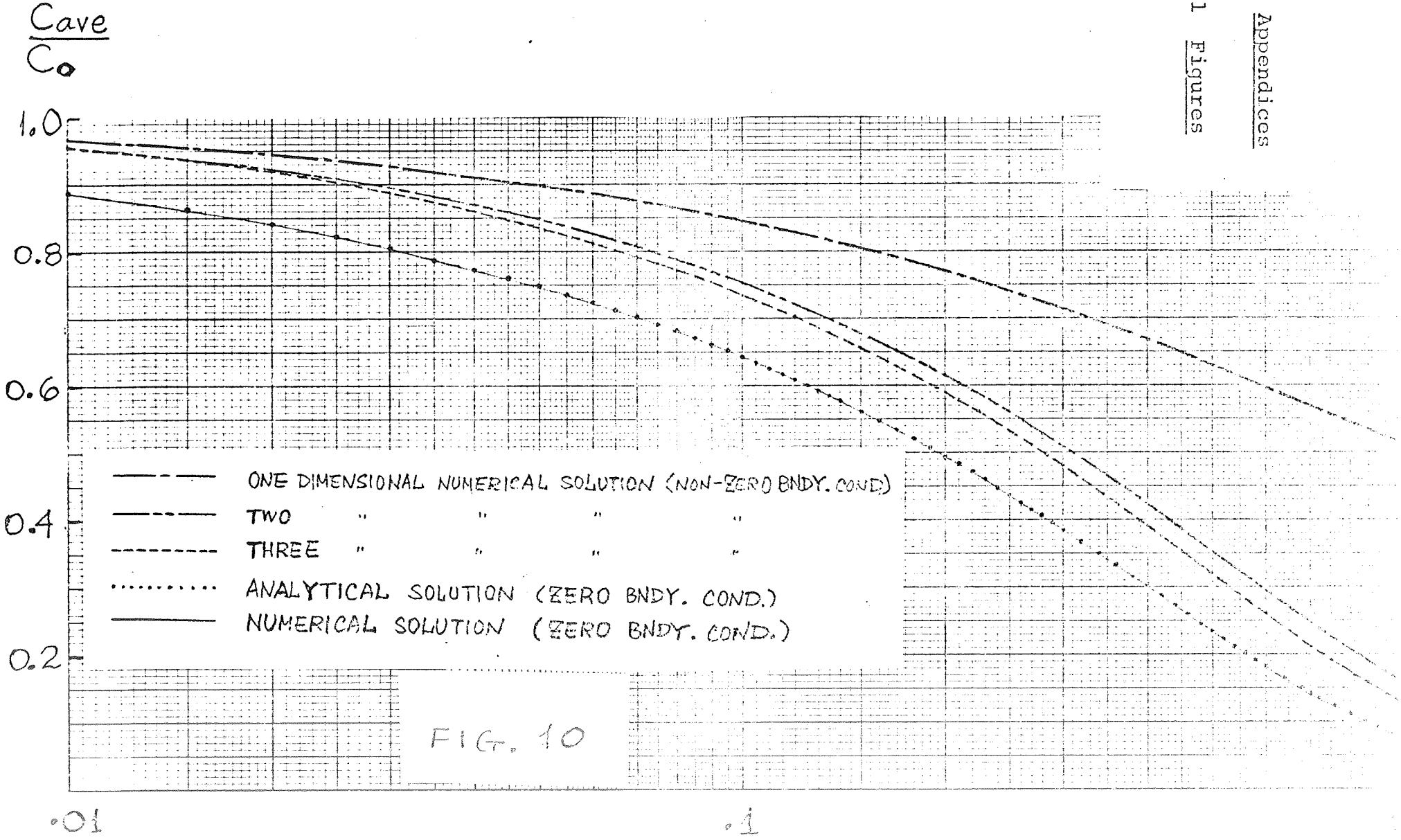
Cave/Co
1.0
0.8
0.6
0.4
0.2
ONE DIMENSIONAL NUMERICAL SOLUTION (NON-ZERO BNDY. COND.)
TWO " " " "
THREE " " " "
ANALYTICAL SOLUTION (ZERO BNDY. COND.)
NUMERICAL SOLUTION (ZERO BNDY. COND.)
.01
.1
τ

FIG. 10

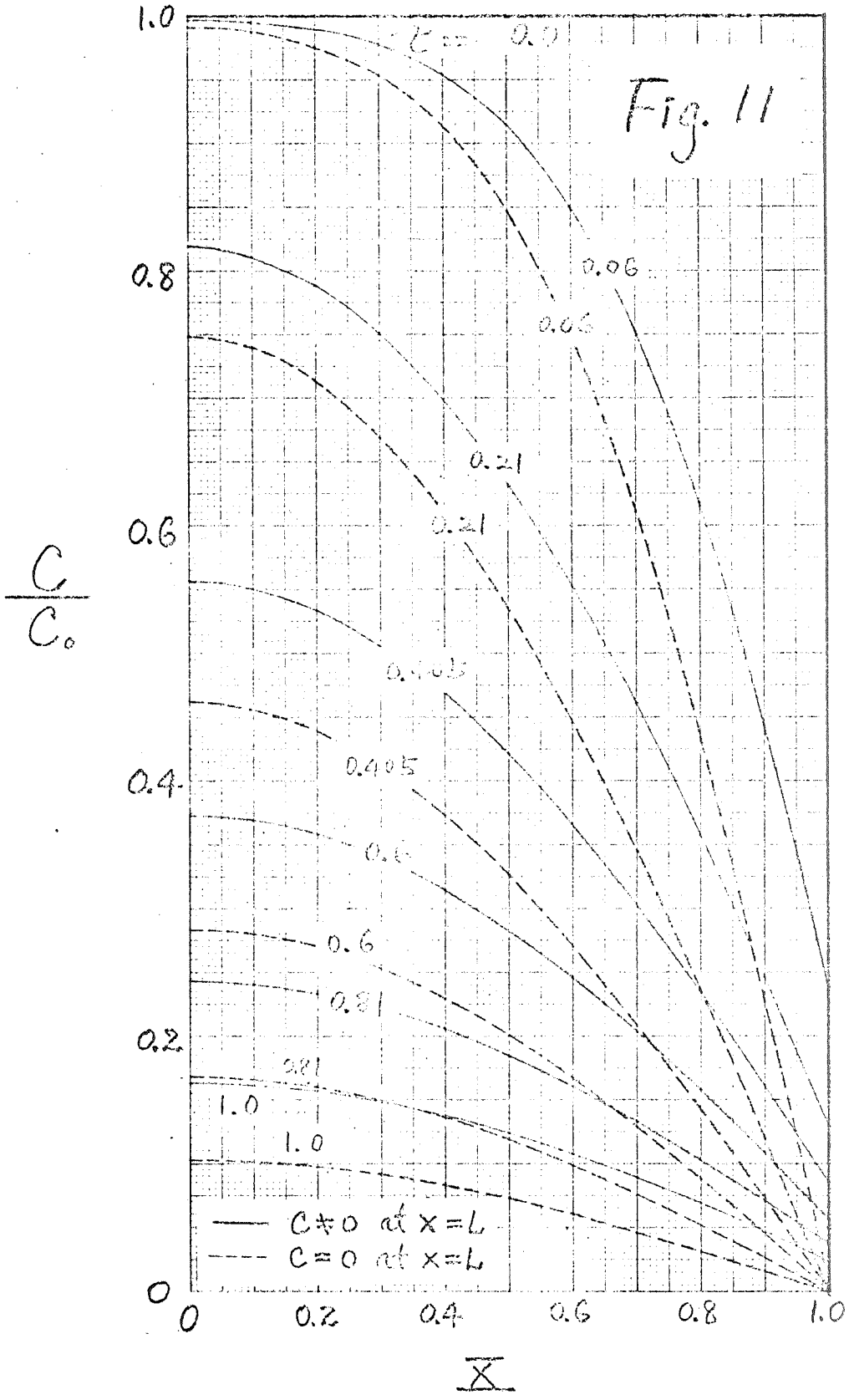
Fig. 11
C/C₀
X
1.0
0.8
0.6
0.4
0.2
0
0
0.2
0.4
0.6
0.8
1.0
0.06
0.21
0.405
0.6
0.81
1.0
C≠0 at x=L
C=0 at x=L

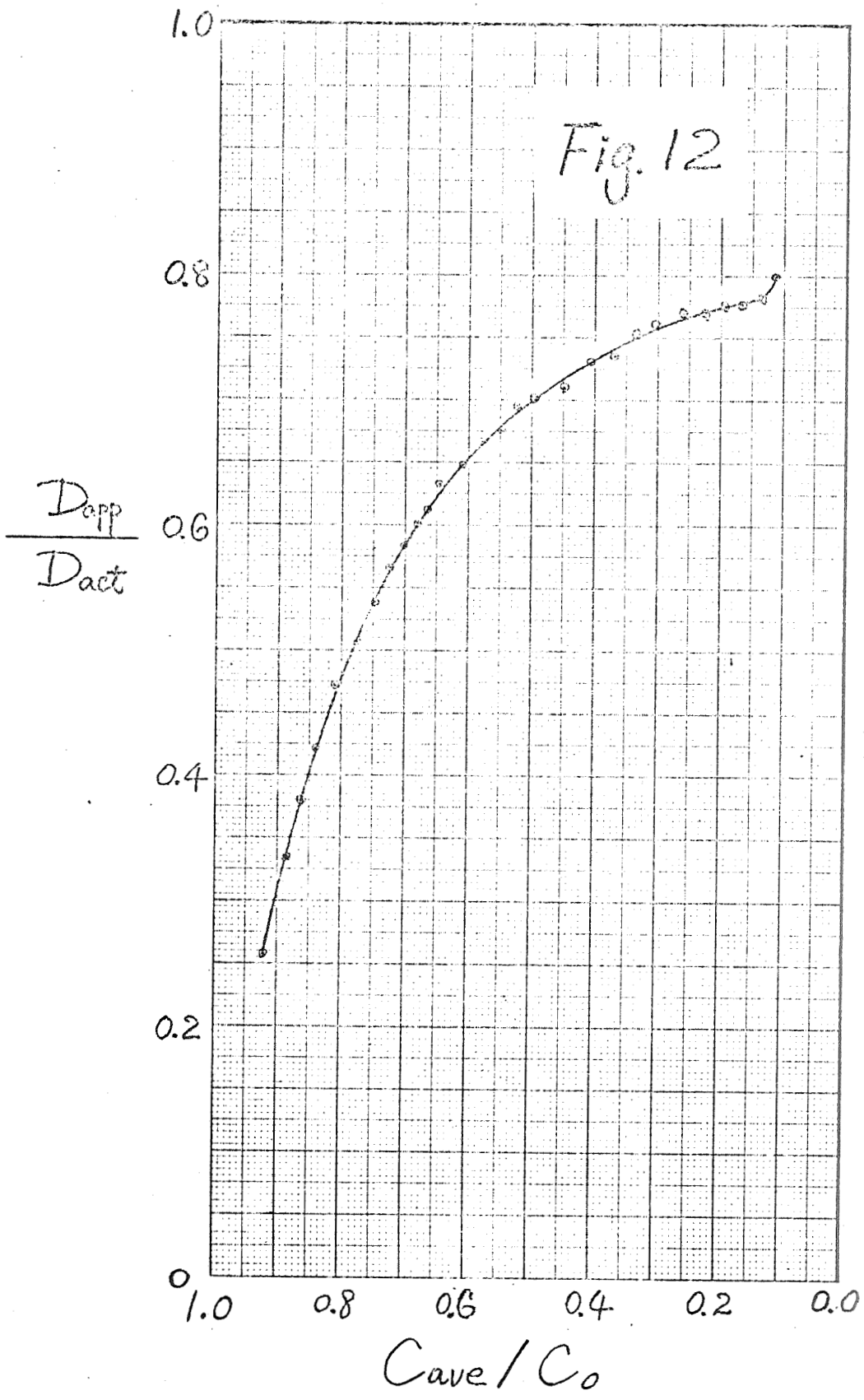
Fig. 12
1.0
0.8
0.6
0.4
0.2
0
Dapp / Dact
1.0
0.8
0.6
0.4
0.2
0.0
Cave / Co

2.2.4.2 References

(1) B. Carnahan, H. Luther and J. Wilkes, Applied Numerical Methods, Wiley, New York (1964).

2.3 Electrolyte Diffusivity Measurements

2.3.1 Introduction

In order to relate membrane diffusivities and activation energies to specific membrane models, it is necessary to have accurate data for ion diffusivities in free liquid. The limiting current at a zinc rotating disc offered the possibility of determining zincate ion diffusivity in KOH for sufficiently large zincate concentration, i.e., 0.25M ZnO in 5M KOH. [1] However, for lower ZnO concentrations, the disc current-voltage curve was masked by simultaneous hydrogen evolution, so that it was difficult to evaluate a clear-cut diffusivity.

The capillary method was initiated in this contract as a means for determining diffusivity in a non-electrochemical way as a check on the rotating disc method and also to provide a diffusivity value independent of electrical field (migration effects). Details of the design, construction and refinement of the capillary flow channel may be found in previous reports. [2] [3]

The salient feature of the flow channel is the controlled low velocity of liquid streaming past the capillary mouth in order to reduce the $\Delta\ell$-effect error. As indicated in the previous reports, the flow velocity was required to be 1.2×10^{-4} cm/sec for a capillary i.d. of 0.2 cm where the expected diffusivity was on the order of 10^{-5} cm^2 sec. In order

to check the apparatus, 1.0N KCl was chosen since the integral diffusivity is known to be 1.86×10^{-5} cm^2 sec^{-1}. A run lasting 65.2 hours was made with the temperature maintained at 25.0°C ±0.4°C. The Reynolds number was constantly monitored and adjusted to be within the range 0.003 to 0.03. Various capillary lengths were used to insure a wide variation in remaining fraction within the capillary. Capillary contents were analyzed by atomic absorption methods. The value for KCl diffusivity was found to be $1.75 \pm 0.05 \times 10^{-5}$ cm^2 sec^{-1} at 25.0°C ±0.4°C.

2.3.2 Capillary Placement

A diffusion run was started by slowly turning nylon screws whose ends covered the capillary mouths. The distilled water flowing in the channel did not completely fill the vertical dimension of the channel, so local velocities were computed on the basis of the actual depth. A fully developed laminar flow was assumed so that the velocity profile in the horizontal direction was considered to be parabolic with maximum in the center as

$$V = V_c \left[1 - \left(\frac{y}{W} \right)^2 \right] \qquad \text{[Equation 1]}$$

and the velocity profile in the vertical direction was taken to be (along the centerline)

$$V_c = V_t \left[1 - \left(\frac{Z}{H} \right)^2 \right] \qquad \text{[Equation 2]}$$

where D = water depth in channel

2W = channel width

V_c = centerline velocity

V_t = surface velocity at centerline.

By substituting Eqn. 2 in Eqn. 1 and integrating to obtain an average velocity, there results

$$V_t = \frac{9}{4} V_{ave} = \frac{9}{4} \frac{Q}{\rho A} \qquad \text{[Equation 3]}$$

where Q = volumetric flow rate, ml/sec

ρ = density, g/cc

A = cross-sectional area of the channel, cm^2.

Finally,

$$V = V_t \left[1 - \left(\frac{y}{W} \right)^2 \right] \left[1 - \left(\frac{Z}{D} \right)^2 \right] \qquad \text{[Equation 4]}$$

By combining Eqn. 3 and 4 and putting $y = 0.7$, $W = 2.3$, $Z = 1.3$, and $D = 2.6$ cm, for the capillary arrangement in the channel one obtains

$$V = .128 \frac{Q}{\rho}$$

where V is the velocity of the fluid in the channel at the mouth of the capillaries. It should be noted that all mouths are at the same Z value and that symmetry about the y centerline exists.

During the experimental run, the velocity was fast enough to satisfy the boundary condition of zero concentration at the mouth of the capillary, but small enough to make the $\Delta\ell$-effect negligible.

2.3.3 Flow and Temperature Monitoring

The temperature in the capillary channel was maintained at 25.0°C ±0.4°C. Continuous monitoring was provided with an amplified signal displayed on a Beckman 1005 10mV Linear Recorder using a copper-constantan (bare metal) thermocouple inserted directly into the capillary channel. An ice bath was used as a reference junction. The average temperature variation was no greater than ±0.4°C over the 65 hour interval. A mercury in glass thermometer was used for the primary temperature measurement of 25.0°C. Control was provided by the circuit described in a previous report. [4]

The flow rate was checked periodically by disconnecting the outlet tubing from the capillary channel overflow head tank and measuring (stop-watch) the time to collect a 5 to 10 ml sample in a graduated cylinder. If the rate was found to be less than 0.01 ml per second, the flow rate was increased by adjusting a needle valve in the inlet line of the capillary channel. The flow was checked at four-hour intervals over the 65 hour time span of the experiment and never exceeded 0.015 ml/sec corresponding to a velocity past the capillary mouths of 2×10^{-3} cm sec^{-1} or a Reynolds number of 0.03.

2.3.4 Analysis of Capillary Contents and Standards

The run was terminated by tightening down the nylon closing screws, draining the channel and removing the lucite capillaries. As mentioned previously (Sec. 2.3.1), the different capillary lengths were 2.54, 3.49 and 4.44 cm, and were

chosen to provide a wide variation of dimensionless time. Each capillary was made with a 1/16 inch i.d. (0.158 cm) and the volume of each was determined by weighing a mercury column which filled the capillary.

After the run was completed, the contents of each capillary was washed out with 60 ml of distilled water using a 10 ml plastic syringe with hypodermic 2 inch needle. The distilled water was previously tested and found to have less than 0.1 microgram of potassium per milliliter, using the Varian AA-120 atomic absorption spectrophotometer. The 60 ml extract was further diluted to either 200 or 250 ml exactly, including all washings from intermediary containers. Finally, the diluted test samples were placed in 250 ml wide mouth polyethylene bottles for use in the AA-120.

Standard solutions were prepared by diluting the same stock 1.0N KCl solution used in the diffusivity measurements. In order to obtain spectrophotometer readings which were as nearly linear as possible, two overlapping calibration curves were prepared to cover the range of concentrations studied. A Leeds and Northrup Speedomax Recorder was attached to the AA-120 so that the individual replicate readings of any sample were obtained and stored on an expanded scale. A reading of a sample consisted of snorkeling the sample into the nebulizer for approximately 10 seconds. The reading on the recorder paper appeared as a fluctuating line well within ±1 absorption scale unit. An averaged value was based on a line drawn through the trace. Complete calibration check runs were

made both before and after a session of capillary contents analyses in order to monitor any possible AA-120 changes due to lamp aging, warm-up variation, etc. A typical sequence is detailed as follows:

(1) AA-120 warmed up for one half hour.

(2) Nebulizer thoroughly cleaned with distilled water.

(3) Machine adjusted for potassium readings in suitable percent absorption range, typically 3.91 to 9.77 µgm K per ml or 1.22 to 4.89 µgm K per ml.

(4) Standard solutions snorkeled ten times apiece. Before a new standard solution was snorkeled, the machine was rinsed with distilled water by snorkeling distilled water for about 20 seconds.

(5) Test samples from various capillaries were snorkeled ten times apiece, rinsing machine with distilled water between samples from different capillaries.

(6) Standard solutions were snorkeled again ten times apiece, rinsing with distilled water between samples.

The average values and standard deviations were determined by using a Hewlett-Packard 9100A Desk Calculator Statistics Program Part No. 09100-7081. Calibration curves were fitted to a straight line by using a Hewlett-Packard 9100A program Part No. 09100-70802 (least squares technique). The least squares results for the K standards fitted the straight line equation

$$Y = MX + B \qquad \text{[Equation 5]}$$

where Y = percent absorption, AA-120 scale

X = concentration (μgm K per ml H_2O)

with excellent correlation factor as shown in Table I for calibrations made with standard solutions before and after analyses of the medium and large length capillaries.

Table I

Least Square Parameters for Standard Calibration Potassium Absorption

Series	B, % absorpt.	M	R (correlation factor)
High Range, Before analysis long, medium capillaries	-11.822	5.279	0.99698
After	-12.34	5.200	0.99854
Low Range, Before analysis, small capillaries	-1.282	8.983	0.99832
After	-1.50	9.006	0.99827

2.3.5 Results

Analysis of capillary contents according to the sequence described in Sec. 2.3.4 were interpolated using Eqn. 5 and the parameters shown in Table I. The actual concentration of the capillary after the experimental run was finished was determined by back calculating from the dilution factor of each capillary (200 or 250 ml) and the volume of each capillary, giving the value of C_{ave}. The initial concentration is, of course, known to be 1.0 N KCl, thus determining C_{ave}/C_o.

The complete solution for the average concentration remaining in the capillary of length L after a time t of

diffusion in a system with the boundary condition of zero concentration provided by flow past the capillary mouth is known to be

$$\frac{C_{ave}}{C_o} = \frac{8}{\pi^2} \sum_{n=0}^{\infty} \frac{1}{(2n+1)^2} e^{\frac{-(2n+1)^2 \pi^2 Dt}{L^2}} \qquad \text{[Equation 6]}$$

where D is diffusivity, $cm^2\ sec^{-1}$. For sufficiently long time, i.e., dimensionless time $Dt/L^2 > 0.1$, all but the first ($n = 0$) term in Eqn. 6 may be omitted as negligible. Thus, Eqn. 6 may be rearranged to give

$$D = \frac{-4L^2}{\pi^2 t} \ln\left(\frac{\pi^2}{8} \frac{C_{ave}}{C_o}\right) \qquad \text{[Equation 7]}$$

so that D, the integral diffusivity coefficient, can be computed from C_{ave}/C_o. Results are summarized in Table II for the two sets of capillaries used simultaneously and for each set based on the calibration curves determined before and after analysis of capillary contents. For both set 1 and 2 (subscripts), the capillary designated L was 4.44 cm long, M was 3.49 and S was 2.54 cm.

Table II

Diffusivity Data
0.1N KCl into pure H_2O, 25.0 ±0.4°C

Capillary	Concentration of Diluted Capillary µgm K/ml H_2O	Concentration in Capillary, end of run µgm K/ml H_2O x 10^4	$\frac{C_{ave}}{C_o}$	D cm^2 s x
		Based on first calibration		
L - 1	8.225	1.862	.476	1.81
M - 1	4.702	1.378	.352	1.75
S - 1	2.048	0.649	.166	1.70
L - 2	8.176	1.875	.476	1.79
M - 2	4.666	1.348	.345	1.78
S - 2	2.050	0.655	.167	1.79
		Based on second (final) calibration		
L - 1	8.450	1.913	.489	1.7
M - 1	4.873	1.428	.365	1.68
S - 1	2.067	0.655	.167	1.7
L - 2	8.400	1.928	.493	1.69
M - 2	4.836	1.397	.357	1.7
S - 2	2.069	0.661	.169	1.74

2.3.6 Discussion

The nature of the hydrodynamic $\Delta\ell$-error is such as to always contribute a positive error to the diffusivity measurement. For the same diffusion time, the shorter capillary should

be most susceptible to error, since the hydrodynamically swept-out volume is the same for all capillary lengths. For a given length, the $\Delta\ell$-effect contributes most to the over-estimate of D for small diffusion time, becoming less of an error as experimental diffusion time increases. Thus, it is noteworthy that no trend is found between the groups 1 and 2 or between lengths in any one group for the data in Table II. Errors are thus considered to be truly random. Based on early calibration curves, the diffusivity of KCl is 1.78×10^{-5} cm^2 sec^{-1} with standard deviation of 0.02×10^{-5}. On the basis of final calibrations, the average diffusivity is 1.72×10^{-5} with 0.03×10^{-5} standard deviation. The combined average value is $1.75 \pm 0.05 \times 10^{-5}$ cm^2 sec^{-1}. On the basis of data compiled by Harned [5], the differential diffusivity of KCl at 25°C starts at the limiting dilute value of 1.99×10^{-5} and drops rapidly to a minimum value (1.835) at 0.2M, increasing thereafter in a nearly linear fashion to 1.893 at 1.0M. Data in the dilute region up to 0.2M were obtained from calculations based on conductivity data, while a two-compartment diaphragm cell was used for diffusivities at higher concentrations. [5] The integral value for KCl at 25°C was determined by graphical integration of Harned's data as 1.86×10^{-5} cm^2 sec^{-1}. On the whole, the agreement is fair, lending credence to the flow channel method. However, a similar discrepancy was also noted earlier in this project [6] where very

short time (4-6 hour) capillary runs were made with 0.1N KCl at 25°C. The value obtained, 1.79×10^{-5} cm^2 sec^{-1}, was less than the differential diffusivity of 1.843×10^{-5} cm^2 sec^{-1} and most certainly less than the integral diffusivity from 0.1N KCl to pure water, estimated to be 1.875×10^{-5} cm^2 sec^{-1}. While the mathematical treatment which leads to Eqn. 6, 7 is based on the assumption of constant diffusivity, the true concentration dependence may have to be taken into account. However, the capillary method leads to a value which is consistently below even the smallest value of D in the given concentration region, whereas some average between the maximum and minimum D should be expected. The cause for this discrepancy is not known and certainly deserves further consideration.

2.3.7 References

(1) Quarterly Report, July-Sept 1970, Sec. 1.2, JPL 952-543.

(2) Quarterly Report, July-Sept 1970, Sec. 2.2, JPL 952-543.

(3) Quarterly Report, Oct-Dec 1970, Jan-March 1971, Sec. 2.2, JPL 952-543.

(4) Quarterly Report, Oct-Dec 1970, Jan-March 1971, Sec. 2.2.1, Fig. 3, JPL 952-543.

(5) H. S. Harned, "Electrochemical Constants," NBS Circular 524 (1953), p. 71.

(6) Quarterly Report, Feb 1970, Sec. 2.2.2, JPL 952-543.